Latest advances in the manufacturing of 3D rechargeable lithium microbatteries

Stefania Ferrari,[a*] Melanie Loveridge,[a] Shane D. Beattie,[a] Marcus Jahn,[a] Richard J. Dashwood,[a] Rohit Bhagat,[a]

[a] WMG, University of Warwick, CV4 7AL Coventry, UK

Corresponding Author
* S.Ferrari@warwick.ac.uk

Abstract

Recent advances in micro- and nano-electromechanical systems (MEMS/NEMS) technology have led to a niche industry of diverse small-scale devices that include microsensors, micromachines and drug-delivery systems. For these devices, there is an urgent need to develop Micro Lithium Ion Batteries (MLIBs) with dimensions on the scale 1-10 mm^3 enabling on-board power delivery.
Unfortunately, power limitations are inherent in planar 2D cells and only the advent of 3D designs and microarchitectures will lead to a real breakthrough in the microbattery technology. During the last few years, many efforts to optimise MLIBs were discussed in literature, both in the planar and 3D configurations.
This review highlights the importance of 3D microarchitectured electrodes to fabricate batteries that can be device-integrated with exceptionally high specific power density coupled with exquisite miniaturisation. A wide literature overview is provided and recent advances in manufacturing routes to 3D-MLIBs comprising materials synthesis, device formulation, device testing are herein discussed. The advent of simple, economic and easily scalable fabrication processes such as 3D printing will have a decisive role in the growing field of micropower sources and microdevices.

Keywords
Li-ion microbatteries, thin film, 3D printing, silicon

Highlights

- In this paper the recent state-of-the-art on lithium-ion microbatteries is reviewed.
- The importance of the development of 3D designs is highlighted.
- Fabrication routes to 3D lithium microbatteries including additive layer manufacturing are presented.
- Materials synthesis, device formulation, device testing are herein discussed.

1- Introduction

In these last years, microscale technologies have gained a lot of importance since a variety of small devices have entered recently in our everyday life and many others that could have an enormous impact, for example, biomedical *in vivo* micro-machines, are waiting for a breakthrough in the miniaturization of power sources to become autonomous devices. So far, there has been little progress in battery miniaturization which has not kept pace with advances of microelectronics, and the demand for batteries in the 1-10 mm^3 volume scale remains high. Lithium Ion Batteries (LIBs) have the highest energy per unit weight of the known energy storage systems and being a mature technology, is a leading candidate for the development of Micro Lithium Ion Batteries (MLIBs) that are able to be integrated in microelectronic devices. Reducing the size of a common LIB requires an update of the traditional manufacturing method of building electrodes and also a careful evaluation of alternative electrolytes compared to conventionally employed liquid ones, to avoid leakage risks and other safety issues [1]. In this regard, both thin-film and thick film all-solid-state microbatteries have been the centre of extensive exploration [2] and have been developed by several start-up companies [see for example refs (3)].

Despite significant achievements in the fabrication and optimisation of thin film microbatteries, limitations in areal capacity and in power densities [4] motivated the research of alternative designs and in particular the three-dimensional (3D) concept that has been recently proposed, is attracting interest. The investigation, production and assembly of all the components of a MLIB in a complete 3D configuration is a particularly challenging prospect and demonstrates the infancy of this technological area [5]. In spite of this, significant results have been recently achieved in this field thanks to a careful design of the microarchitecture [6] and/or to the fabrication method [7].

In recent years there have been some high quality review articles on 3D microbatteries [1, 8-10] that gave a comprehensive description of the 3D concept and potentiality. A range of fabrication methods was covered and emphasis was placed on electrodes architecture and on some deposition techniques, such as electrodeposition [10]. The ongoing research in this field has recently seen the advent of innovative manufacturing processes such as 3D printing [7, 11-12], of mathematical modelling to investigate ionic transport in 3D electrodes [13-16] and of interesting materials such as silicon, which could play a key role in the development of high energy density devices.

In this review article we focus our attention on the relationship between battery chemistry and fabrication/integration of the battery components, and on the innovations in manufacturing

that have contributed to the developments of some successful high performance miniature power sources. After a general overview of thin/thick film MLIBs, 3D-MLIBs and their advantages over the planar counterpart will be discussed. The different designs proposed so far in the literature and the different fabrication approaches are carefully reviewed to highlight the influence of the manufacturing method on the electrochemical performance of the battery.

2- Microbattery Technology Overview

Currently, primary macrobatteries (greater than 1 cm^2) are the prevalent power source for wireless sensors and integrated systems. Their relative low cost has made it difficult to replace them by emerging technologies. However, with growing demand for design freedom and miniaturisation of devices, integrated microbatteries, especially rechargeable ones, have gained significantly more attention in recent years. Secondary microbatteries based on different chemistries have been proposed as integrated micropower systems for a variety of applications: Ni-Zn, manganese alkaline, zinc-silver alkaline and other chemistries.

The operating mechanism of a MLIB is exactly the same as for a classical LIB; two electrodes (positive and negative) are separated by an electrolyte layer. The main difference between standard LIBs and MLIBs is the size of the battery which should be of the order of ≤ 0.1 cm^3. Consequently the energy and power densities depend not only on the chemistry but on the dimensions and geometry of the device. Some impressive performances have been reported recently (see following sections), however most of the microbatteries including commercial ones shows volumetric energy and power densities in the range 0.1-1 $Jcm^{-2}\mu m^{-1}$ and 0.0001-10 $mWcm^{-2}\mu m^{-1}$, respectively. The energy requirements of some mobile devices can span from tens of nanowatts to tens of milliwatts, as shown in Figure 1. Should be noted that when scaling down a power supply, the contribution of inactive materials, for example that used for packaging the battery, on the total mass and volume becomes significant. For this reason, all the components that could add inactive mass and complexity to the manufacturing process have to be carefully reviewed. In this sense, all-solid-state microbatteries have emerged strongly because they do not need separators, the packaging can be simple and integrated with current collectors and electrodes, and are intrinsically safe. In addition, the developments in the field of solid state ion conducting materials both ceramic and polymeric contributed to the innovation and achievements in all-solid-state microbatteries.

2.1 – Thin and thick film microbatteries

The term “thin film” is often found ambiguous in literature, but in agreement with most definitions, films of <1μm can be considered thin films. However, for the purpose of this review, a thickness of less than 10μm is considered as “thin” since this will make a clear distinction between traditional electrodes deposited by slurry casting and electrodes suitable for microbatteries.

2D thin film batteries usually consist of multiple layers deposited sequentially either in a planar or stacked arrangements as shown in Figure 2a) and b). In planar batteries, positive and negative electrodes are positioned next to each other on the same non-conducting substrate. Being physically disconnected there is no need of separators between them. This kind of cells can either be simply submerged in a liquid electrolyte or covered with a solid one. Both cases will need an encapsulating layer, usually an inert polymer. One of the major drawbacks of this design is that the current density distribution across each electrodes depends on the relative distance from the adjacent electrode, thus leading to power failures during fast charging and discharging of the cell. Moreover, thin film planar batteries often require rather large footprints in order to deliver acceptable capacity and energy. The cathode active volume limits the capacity of the battery that is given by the footprint area multiplied by the cathode thickness (cathodes are typically few micrometers thick). For example, the measured capacity of a cell 2 cm long, 1.5 cm wide and 15 μm thick (cathode $LiCoO_2$ and anode Li metal) was about 400 μAh [17].

Stacked thin film batteries are assembled by depositing consecutive layers on the same footprint area (see Figure 2b), on a layer by layer deposition basis. In this case, the current distribution runs perpendicularly to the overall thickness ensuring a constant performance. For a range of deposition methods thin film electrodes are fabricated without any binders and additives and so, although the chemistry can be the same as with macrobatteries, a substantial difference in the electrochemical performance can be found which depends on processing methods. Several different deposition techniques are available for the fabrication of both planar and stacked thin film microbatteries, such as sputtering, pulsed laser deposition (PLD), chemical vapour deposition (CVD) and sol-gel method. An all-solid-state Li/LiPONB/TiOS MLIB has been recently manufactured at the pilot scale on a Silicon substrate by consequentially depositing all the layers by sputtering and thermal evaporation. Finally, the encapsulation of the battery based on a polymer metal multilayer, was achieved by chemical vapour deposition and sputtering [18]. Such a MLIB worked for more than 1000 cycles at 100% depth of discharge. Should be noted that a drawback of this cell could be the high processing cost due to the rather expensive deposition plants and low deposition rate.

A variety of cathode and anode materials have been deposited and tested so far for the application in thin film macrobatteries such as LiMO-type materials ($LiCoO_2$ and $LiMn_2O_4$), olivine and polyanion materials ($LiFePO_4$, $LiMnPO_4$ and $LiNiVO_4$), metal oxides and metal nitrides for the positive and Sn-M alloys, silicon and lithium (the latter one for all-solid-state batteries) for the negative electrode. A comprehensive review [19] on nanostructured thin film electrodes for thin film lithium batteries has been recently published where relevant information on progress in research in this field can be found.

After the first prototypes of thin film MLIBs were successfully established, requirements for higher energy densities led to the development of thick film MLIBs where the electrode thickness is approximately on order of magnitude higher than in thin film ones.

Thick film MLIBs (total thickness including packaging in the range of 50-1000 μm) were the first step towards increasing the active cathode volume to achieve higher areal energy densities. It was found that the energy per footprint area increased with the thickness of the cathode, however the mechanical integrity of the film decreased with the thickness, as the active material expands and contracts during cycling. The power density for thicker films is also reduced due to the increasing influence of the slow diffusion of Li ions so that in general for stacked microbatteries one has to find the right compromise between energy and power density.

The fabrication processes are numerous; for example in case of microfabricated thick film MLIBs methods are similar to those used for integrated circuits and MEMS devices. Solution processed MLIBs are usually based on electrodes deposited by solution-based methods. Direct write fabricated MLIBs have also been developed and since they do not require photolithographic processing steps, are a cost effective and straightforward alternative. The convenience of the laser direct-write process has been demonstrated through the fabrication of both a planar primary Zn-Ag_2O and a secondary MLIB [20] and confirmed recently by Kim et al (see Figure 3a) [21]. The MLIB fabricated in this work employed $LiCoO_2$ as cathode, carbon as anode and a gel polymer electrolyte GPE based on PVdF-HFP, and could achieve a maximum power density of approximately 38 mW cm^{-2} with a 68 μm thick cathode [21]. The microinjection technology is another method of direct writing that allows the deposition of small volumes of inks (tens of picoliters), so that electrode microarrays can be fabricated. In Figure 3b, an example of a cell fabricated by a sol-gel method combined with microinjection is shown [22]. An all solid state MLIB was then fabricated and successfully operated at ambient temperature using a PEO based polymer electrolyte.

2.2 – Commercial MLIBs

Microbatteries are among the key enablers of miniaturised high-performance power sources for micro electric systems. It is estimated that the MLIB market could be worth up to $1.5bn by 2017 with an impressive $34.6 billion predicted revenue for 2021 from point-of-care diagnostics alone. With more application emerging on a regular basis, micro-electronics are nowadays far beyond the traditional portable consumer electronics alone. Micro-drones, smart wearable electronics and lab-on-a-chip devices are becoming more sophisticated and are already commercially available. These devices usually do not require large energy densities as drawn currents are comparably small (in the order of μA). However, power densities are often critical and have led to extensive research efforts to improve the cell design and manufacturing process to enable higher power densities and ever smaller, lower profile and flexible micro devices. Among several theoretically designed micro architectures [1], only few designs have been experimentally realised with even fewer found commercially viable (see Table 1 for some commercialised MLIBs and their features). Several battery chemistries have been used in the past for microbatteries designs with primary batteries still playing a large role for most applications due to fewer available Li ion alternatives in comparison to larger scale batteries.

Most commercially available as well as laboratory scale MLIBs rely on radio frequency (RF) magnetron sputtering for thin film deposition. The deposition of metallic Lithium is especially challenging and its use emphasises the need for more advanced research in the area. Although the use of Li metal is of less concern to most applications for MLIBs and the risk of dendrite growth is significantly reduced by employing all-solid-state battery design, replacing Li metal remains a major challenge, since its specific capacity and high electrochemical potential are crucial for the feasibility of practical microbatteries.

2.3 – Integrated MLIBs

One of the major challenges in the microbattery field is related to the manufacturing process and its compatibility with the integrated circuit technology [23-24]. Typical thin-film processing requires high temperature (500-900°C), and masking and etching incompatible with chip materials and packages. For these reasons, it is necessary to find alternative fabrication routes to obtain fully integrated systems.

A concept has been developed at Fraunhofer IZM which combines state-of-the-art LIB materials with wafer-level processing, in the attempt to overcome the main limitations of thin film microbatteries (low capacities and high battery price) [24-25]. The size vs. energy range of this model is shown in Figure 4a compared to lithium polymer, coin cell and thin film

batteries [26]. At first, prototypes on a laboratory scale were fabricated; battery laminates were cut into mm-sized pieces and placed into Si cavities and hermetically sealed beneath a glass lid. The battery cavity (200 μm deep) was etched into the Si substrates by means of reactive ion beam etching. Active materials of the stacked electrodes were $Li_{(1-x)}(Ni)CoO_2$ and Li_xC_6. A near hermetic packaging was realized with the help of a UV curable epoxy seal. These prototypes achieved a capacity of 3 mAh cm^{-2} with a reduction in capacity of approximately 10% after 100 cycles, and an energy density of 10mWh cm^{-2}. During the early development of this technology it was found that that design gave unreliable electrical contact, as this was dependent on the contact pressure between the battery substrate and the battery lid [25]. Other shortcomings were related to the easiness of mechanically damaging the encapsulation layer and to the partial loss of the organic electrolyte solvent during the vacuum processing for the encapsulation. To overcome such limitations the MLIB design was modified [26]. To make the battery assembly easier, anode and cathode were fabricated side by side in a planar arrangement. In this design Li ions move laterally from one electrode to the other crossing a silicon spacer (see Figure 4b) [27]. The slurries of active materials ($LiCoO_2$ and graphite) were inserted into the cavities by volumetric micro dispensing. The batteries were closed using a glass lid with holes for the filling of the liquid electrolyte and successive removal of the gas generated during the formation. The cells integrated on a chip (see Figure 4c) were completely sealed after the formation and then tested up to 5C rate. A linear capacity loss rate of < 1% per cycle over 30 cycles at a rate of 0.1C was observed.

3. 3D-MLIBs

In recent years, the need to rethink the electrode design is becoming more evident, in order to achieve a marked improvement in the performance of electrochemical power sources. In particular, it is generally agreed that a tailored dimensionality is the key to push forward energy and power density [28]. 2D battery systems simply cannot provide sufficient power for a variety of small power applications such as, for example MEMS devices. Multifunctional 3D nanoarchitectures are expected to offer several advantages for energy storage and conversion such as short transport length for ions, interpenetration among active components, small areal footprint and especially small devices could gain enormous benefits through a redesign from 2D to 3D. The quantitative advantage offered by the 3D configuration over the conventional 2D one was proved through calculation for a 3D interdigitated electrode array (Figure 5a); the energy capacity of a 3D design will always be lower than that of a 2D design for equal total volumes, but transport length is more than 300% higher for a 2D configuration

and an increase in areal energy capacity for the 3D battery can be easily obtained without loss in power density, simply by increasing for example the height of an interdigitated battery [29]. The area enlargement factor or area gain is normally used to quantify the gain obtained with the 3D design compared to the 2D, and is the ratio between the 3D and 2D surface areas.

Several 3D architectures have been proposed so far, the most common ones are shown in Figure 5. The first one is based on interdigitated electrodes in form of pillars or rods (Figure 5a), in which anode and cathodes nanorods alternate to form ordered arrays separated by the electrolyte. The trench design (Figure 5b) is constituted by interdigitated plates rather than rods and was first practically demonstrated by Notten et al. [30, 31] who developed an all-solid-state MLIB having this configuration. In the concentric 3D architecture (Figure 5c) the electrodes volume is fully utilised, the volume occupied by the electrolyte is minimised so that the obtainable energy density is increased. Rods of one or the other active material are coated by an electrolyte layer and the remaining volume is filled by the other electrode material. Finally, the aperiodic or sponge design (Figure 5d) is not based on a regular structure but consists of a randomly oriented network of electrode materials onto which the electrolyte is deposited. These structures, typical of aerogel-like architectures, are characterised by a very large surface-to-volume ratio and also by a high risk of short-circuits between the cathode and the anode, due to the possible formation of holes in the extremely thin separator layer. Among these 3D designs, the interdigitated ones are generally considered to be more straightforward to manufacture. Nonetheless, the risk of causing short circuits due to electrode volume change and pinhole formation during battery cycling is significant and crucial to the overall design. A trade-off between increased energy densities and increased risk of short circuiting by decreasing the distance between electrodes becomes apparent.

In general, two categories of 3D-MLIBs have been proposed until now, the first one can be defined as a free-standing battery (see next paragraph) and the second one makes use of a perforated substrate to fabricate a battery based on microchannel plates [1]. In this latter type, all the battery components (electrodes, electrolyte and current collectors) are deposited conformally on the top, bottom and internal hole surfaces of the perforated mold, taking advantage of the deposition methods commonly used for the fabrication of thin film batteries. A disadvantage of this configuration is that the inactive material of the 3D substrate contributes significantly to the overall volume and limits the energy density of the battery.

3.1 – Nanostructured current collectors

The first step towards the fabrication of a free-standing 3D-MLIB is the manufacture of the base array that acts as the mechanical support and sometimes also as the three-dimensional current collector. To ensure an efficient current distribution, an architectured current collector should have agglomerates that are evenly spaced and homogenous in size. The most common type of current collector is based on nanowire arrays, submicron-sized rods that are produced directly on metal substrates. Arrays of freestanding Al, Cu and Ni nanorods (see Figure 6a and b) are often fabricated by constant current and pulsed current electrodeposition [10, 32-34]. The pulsed approach, promoting grain nucleation, is the preferred one to obtain a narrower height distribution for the rods, with the length of the rods being controlled by the deposition time. Porous alumina membranes and polycarbonate membranes are often used as a template for the electrodeposition of the rods since they are easily dissolved to obtain freestanding current collectors. The space between the nanorods (pore size) in this structure is typically around 50-200 nm depending on the interpore distance in commercial alumina membranes. Ionic liquids (ILs) such as [EMIm]Cl or [EMIm]TFSI (1-ethyl-3-methylimidazolioum chloride/bis(trifuoromethylsulfony)limide) have been shown to be an ideal electrolytic bath for the electrodeposition of Al from $AlCl_3$, since it can be performed only in non-aqueous solvents [10, 32, 35]. Moreover, by using ILs, a structured Al current collector was electrodeposited onto Al substrates without the need of a template [35].

Recently, Au nanoporous nanorods exhibiting two different levels of porosity have been demonstrated as current collectors for 3D-LIBs [36]. Each nanorod had high surface area and (pore size less than 10 nm), while the space between the nanorods was in the range 50-100 nm. This configuration accommodated more mass per unit geometric area leading to improved rate characteristics compared to nanotube and nanorod design.

A new way of looking to the architecture of 3D electrodes to overcome reaction kinetics barriers between the active material and the current collector led to the concept of built-in nano-current collectors [37-38]. A nickel nano-current collector was fabricated by means of self-assembled viral templates (Tobacco Mosaic Virus TMV) and provided the support for the successive deposition of the active material [37, 39]. These nano-current collectors act as a metal core that facilitate electronic transfer between the active species and the main current collectors at the terminal. They can also have other positive effects such as relieving the stresses of lithiation/delithiation and assuring the mechanical integrity of the nanorods. A similar approach made use of an electrically conductive bicontinuous Ni scaffold onto which the positive and negative electrodes were electrodeposited. This configuration led to a MLIB exhibiting a power density comparable to that of a supercapacitor [6].

Microfabrication of high-aspect 3D carbon structures (C-MEMS) through photolithography was demonstrated as a viable way to obtain both carbon current collectors and carbon anodes for microbatteries [40-41]. Starting from an epoxy-based negative tone photoresist (SU-8), after a two-step pyrolysis process a variety of complex 3D C-MEMS structures (posts, wires, bridges, plates and ribbons) were built [40]. Figure 6c and d show an array of carbon microrods obtained after pyrolysis and a two level C-MEMS electrodes with carbon contact, respectively. In the two-layer structure, one layer of carbon is the current collector for rows of anode, while the second layer constitutes the cathode posts.

Reticulated carbon structure and carbon felt strands possessing high void space were also used as current collectors and are suitable for the fabrication of MLIBs with an aperiodic design [42-43].

3.2 – Nanoarchitectured 3D cells and electrodes

Although numerous electrodes, both positive and negative, have been developed for the application in microbatteries only few examples of complete 3D cells (not using Li metal as anode) were reported in the literature, mainly due to the complexity involved in assembling miniaturized systems. The research interest has been focused not only on conventional battery materials such as $LiCoO_2$, $LiMn_2O_4$, V_2O_5, $LiFePO_4$ and carbon but also on less conventional and back in vogue/emerging electrode materials such as MoS_2, CuS, FeS, polyaniline (PA) and polypyrrole (PPYDBS) as cathodes, and Cu_2O, TiO_2, SnO_2, Cu_2Sb, $H_2Ti_8O_{17}$, silicon and hybrid or core-shell structures as anodes.

3.2.1 3D-MLIBs supported on perforated substrates

One of the first examples of a 3D rechargeable Li-ion microbattery manufactured by using a perforated substrate (silicon or a glass microchannel plate) was based on an electrodeposited MoS_2 cathode, a lithiated mesocarbon microbeads (MCMB) anode, and a hybrid polymer electrolyte based on PVDF (see Figure 7a and b) [44]. The current collector, cathode and polymer electrolyte layers were thin conformal films deposited on all the available surfaces of the microchannel plate. The cell displayed an operating voltage of 1.5V and a capacity of 2 mAh/cm^2, about 30 times higher than a 2D battery with the same chemistry and footprint area (see Figure 7c). The same research group studied the electrochemical behaviour of semi-3D concentric microbatteries depositing molybdenum oxysulphide, iron sulphide [45-46] and copper sulphide [47] on perforated silicon substrates. Using CuS, the battery provided a specific power of 50 mW/cm^2 and capacities of 1.0-2.5 mAh/cm^2.

A trench design has been then proposed [30-31] which makes use of a silicon substrate covered with a thin layer of TiN to protect Si from Li-ion penetration. The other battery components were a silicon anode, a solid electrolyte and a thin film of a transition metal oxide as cathode (i.e. $LiCoO_2$). These authors focused their experimental work on the diffusion barrier layers, studying Ta, TaN and TiN films as suitable candidates, and on silicon thin film as anode. They also showed that using an inorganic solid electrolyte (LIPON) to cover Si instead of a liquid one the capacity of the electrode did not degrade and was close to the theoretical one for 60 cycles (3500 $mAhg^{-1}$).

This previous work inspired another interesting design that has been recently developed consisting of a silicon microtube scaffold into which one could conformally deposit all the battery components (see Figure 8a) [48]. Prior the fabrication of the scaffold, the area enlargement factor was calculated for different geometrical parameters (outer diameter, inner depth and structure pitch) to optimize the 3D-MLIB. Then, using photolithography and deep-reactive ion etching, a silicon scaffold consisting of microcontainers and micropillars was fabricated in which both the spacing between two microstructures and the microtubes inner diameter were fixed to 1 μm (see Figure 8b). A Pt current collector and TiO_2 anode were deposited into the silicon scaffold by using atomic layer deposition (ALD) (see in Figure 8c the SEM image of the microtubes after the deposition) and half cells with a liquid electrolyte were assembled and tested. An eightfold increase of the surface capacity of the 3D topology was observed compared to a 2D one having the same TiO_2 layer thickness (60 nm).

The use of silicon micromachining techniques has revealed of great importance for the manufacturing of high aspect ratio electrode arrays that could be easily integrated in MEMS devices [40, 49]. The process named C-MEMS (discussed also in the previous paragraph), allowed the manufacturing of 3D anodes and of combined microstructures coated with MCMB particles [50]. 3D interdigitated arrays of Ni and Zn were fabricated by micromolding and subsequent etching of the mold and then used to build a functional battery [49]. Vanadium oxide nanorolls and MCMB electrode arrays prepared in the same way, showed a reversible intercalation of lithium [49]. The C-MEMS fabrication process was also extended to the preparation of a positive electrode array of PPYDBS deposited on carbon rods. A prototype carbon/PPYDBS 3D secondary battery with a standard liquid electrolyte was assembled and cycled galvanostatically at a discharge rate of 20 μAcm^{-2} (0.46C) [41]. The obtained areal capacity was only one third of the calculated one (10.6 μAcm^{-2}) and after three cycles there was evidence of electrical shorting. However, this is one of the few attempts of fabrication of a complete 3D-MLIB.

Very recently the silicon micromachining method has been combined with slurry processing of carbon electrode materials to obtain a robust 3D carbon array [51]. The fabrication process was developed in four steps (see Figure 9a). The channels in the silicon mold were filled with a slurry made of MCMB, carboxymethyl cellulose (CMC) binder, graphite and Ketjen Black (83:7:8:2 wt%). Highly ordered and mechanically robust electrodes were produced, constituted by arrays of carbon posts with different aspect ratios (see Figure 9b). These electrodes were cycled in half cells and although the capacity faded with cycling due to lithium depletion from the electrolyte, exhibited coulombic efficiencies of 95-98% and capacities greater than 5mAhcm^{-2}.

3.2.2 Self supported 3D-MLIBs: template synthesis

Template synthesis (anodic aluminium oxide (AAO) and colloidal crystal template, and bio-template) is the most common approach for the fabrication of 3D self-supported electrodes and consists in the replication of a rigid template material which possesses a specific porosity. AAO is based on the use of a nanoporous anodic alumina membrane template that is etched away once the current collector has been deposited on it. This technique has revealed as a powerful nanofabrication strategy since it allows to obtain materials with precisely controlled sizes, shapes and configuration in a cost-effective way [52].

Mainly negative electrodes have been prepared by using this technique and, as far as we know, a complete battery comprising a cathode also made by AAO has not been fabricated yet. A common strategy is the growth of metal pillars used as current collectors followed by the deposition of the active material on them. For example K. Edström's group developed a method to deposit TiO_2 using ALD on Al nanorods [53] and CuO_2 via electrodeposition on Cu nanopillars, showing in this latter case that CuO_2, which undergoes a conversion reaction, can work well when directly wired to an underlying 3D Cu current collector [42, 54]. Similarly, a 3D Ni/TiO_2 core-shell nanowire network structure was fabricated by electroplating of Ni in a 3D porous alumina template with an inter-channel distance of about 400 nm, a nanochannel diameter of 200-250 nm and side-hole diameter of 50-80 nm, and subsequent ALD of TiO_2 [55]. The authors showed that compared to straight Ni/TiO_2 nanowire arrays prepared using conventional AAO, the 3D nanowire network had a very stable structure and a significantly higher discharge capacity. The cycling performance of a 32 μm long 3D Ni/TiO_2 nanowire network is shown in Figure 10a. The electrode could work for overall 600 cycles and for 500 cycles at 5C discharge rate delivering a stable capacity of 0.06 mAh cm^{-2}. SEM images (see Figure 10b) of a cycled electrode did not show significant

structural changes of the electrode compared to the as prepared one, confirming the high structural stability.

Taking advantage of the AAO fabrication method, engineered nanoelectrodes of tin monosulfide (theoretical lithium storage capacity 782 mAh g^{-1}) have been grown on a copper core, thus overcoming the poor interfacial adhesion shown previously by SnS thick films, easily peeled off from a planar metal substrate [56]. Different experimental conditions were adopted in order to optimize the active material loading and to prevent the formation of a large void space between aggregated nanowire bundles. In addition to the fabrication of the Cu@SnS nanowire arrays, CuS/SnS nanotube arrays were obtained by increasing the reaction temperature. Every hybrid nanowire comprised a Cu core (see Figure 11a) directly connected to the substrate to assure a good electrical contact, and at the reaction temperature of 65°C it was possible to obtain a tubular nanostructure (Figure 11b). The 3D patterned Cu@SnS nanoelectrode achieved a capacity of 451 mAh g^{-1} at 1C and a coulombic efficiency above 99%, showing good reversibility (Figure 11c).

Concerning the fabrication of positive electrodes through AAO template, the sol-gel method is an easy and economical way often used to prepare nanostructures. Among the most commonly used cathode material, $LiCoO_2$ has high capacity and good cyclability and for these reasons was chosen for the fabrication of 3D nanostructured electrodes [57]. In this work, vertical arrays of Al nanorods were at first grown onto Al substrate by the pulsed-potential electrodeposition technique. Then, the sol-gel precursor of $LiCoO_2$ was spray coated onto the Al arrays and annealed at 650°C. At the same time, a 2D planar electrode was also prepared following the same procedure in order to compare the electrochemical performance of the bi-dimensional and three-dimensional structures. The nanostructured 3D electrode demonstrated an excellent rate capability and a two-fold increase in areal capacity with respect to the planar one.

The sol-gel template synthesis was also used to prepare nanofibers of SnO_2 within the pores of a microporous polycarbonate template membrane [58]. The template membrane was simply immersed for 24 hours into a tin oxide-based sol and then placed on a Pt foil current collector. Finally, the polycarbonate template was burnt in an oxygen plasma. SnO_2 undergoes a conversion reaction with Li^+ to form Sn which then can further react with Li^+ to give an alloy $Li_{4.4}Sn$ (maximum theoretical storage capacity of the Li-Sn system is 994 mAh g^{-1}). However, large volume changes accompany the alloying/dealloying process leading to loss of capacity during cycling and to damage of the electrode. Interestingly, these nanofibers of SnO_2 showed

a remarkable performance since they could sustain 1400 cycles at a rate of 58C and delivered a capacity close to 600 mAh g^{-1}[58].

Biotemplating is another template synthesis method that has become a valuable means of micro and nano-fabrication. As discussed previously, metal current collectors can be fabricated by means of self-assembled viral templates [35, 36, 59-60]. TMV (Tobacco Mosaic Virus) is a cylindrical virus about 300 nm long with an outer and inner diameter of 18 nm and 4 nm respectively. TMV templates have been genetically modified introducing cysteine residues to promote covalent-like interactions between the thiol group and metal ions, so enabling metal coating in electroless plating solution and self-assembly onto various surfaces. Using this strategy, positive and negative electrodes comprising a metal core have been fabricated. One of the first examples was a 3D TMV assembled silicon anode [36] that was fabricated by vertically aligning the virus on a stainless steel current collector followed by electroless plating of Ni and finally PVD of silicon. TEM images (see Figure 12a) clearly revealed the different layers of Ni and Si uniformly deposited onto the virus rod. The as prepared anode was tested in a coin cell against a lithium foil, using a standard liquid electrolyte, and achieved a capacity of 3343 mAh g^{-1} at 1C and of 2251 mAh g^{-1} at 2C (see Figure 12b), and coulombic efficiencies approaching 100%. The authors attributed this remarkable cycling ability to the multilayer nanostructure of the anode and notwithstanding the observed volume expansion of silicon after repeated cycling, silicon remained well connected to the Ni core which helped in alleviating the stresses of its expansion. In a similar way a multi-layered C/$LiFePO_4$/Ti/NiTMV1cys nanoforest was fabricated, as shown schematically in Figure 12c, and tested. In this case an additional layer of Ti was deposited by r.f. magnetron sputtering to protect the Ni layer from oxidation during charging and to avoid its diffusion into $LiFePO_4$ [60]. $LiFePO_4$ was coated with a layer of carbon 8nm in thickness. The electrode was then subjected to a high rate testing protocol (Figure 12d) and its performance was compared to those of a 3D nanoforest without carbon coating and of a 2D $LiFePO_4$/Ti thin film cathode having the same active loading but a three times larger thickness of active material (600 nm instead of 200 nm) than the 3D ones. The 3D C/$LiFePO_4$/Ti/NiTMV1cys nanoforest could deliver 84% and 72% of its capacity at 0.1C and 10C respectively, compared to 20% at 0.1C for the 2D electrode. A modified approach which combined bottom-up self-assembly and top-down micromachining made use of a silicon wafer as substrate and a positive photoresist as the electroplating mold to prepare high aspect ratio gold micropillars, then covered with TMV and Ni. The V_2O_5 active material was then deposited by ALD [59].

Along with the use of TMV, also peptide assembly was employed to prepare a nanonetwork structured electrode with a precisely controlled morphology [61]. Hollow nanoribbons with a tunnel cross-section 100-200 nm in width and 20-50 nm in height were fabricated combining peptide-templating (using an organo gel based on diphenylamine) and ALD of anatase as negative electrode active material. The TiO_2 nanonetwork electrode demonstrated excellent cyclability, retaining about 83% of its initial specific capacity after 200 cycles.

Colloidal crystal template is another convenient chemical method to fabricate ordered porous materials with interconnected pores. In general, the interstitial space between closed packed spheres is filled with the target material and then removing those spheres, a negative replica of the original structure is obtained. Three dimensionally ordered macroporous materials (3DOM) called also inverse opals can find numerous applications thanks to their bicontinuous structure [62]. Complete cells were fabricated by using this method.

A recent example of this is a 3D-MLIB fabricated from interdigitated 3D bi-continuous nanoporous electrodes [6] that were obtained starting from a nickel scaffold fabricated by electrodepositing Ni through a polystyrene (PS) opal self-assembled on a glass substrate with interdigitated gold templates. After removing the PS, the NiSn anode, and the $LiMnO_2$ cathode, were obtained by electrodeposition of a nickel-tin alloy and of MnOOH on the nickel scaffold, followed by immersion in molten lithium salts to obtain the lithiated manganese oxide (see Figure 13). The full battery had a volume of about 0.03 mm^3 and an impressive power density of 7.4 mW $cm^{-2}\mu m^{-1}$ was achieved for a cell cycled at 870C rate, well above those reported previously. The authors of this work compared, in a Ragone plot, the performance of their microbattery to those of conventional power technology including supercapacitors. They showed that the 3D-MLIB could deliver 10x the power of a supercapacitor at similar energy density or 10x the energy of a supercapacitor at comparable power density [6].

In a similar way, a Si-on-Ni inverse opal structure was prepared at first by electrodeposition of Ni into the interspace of a PS template and finally of a silicon layer on the Ni inverse opal (see Figure 14) [63]. The authors demonstrated that the 3D bi-continuous transport pathways provided by the inverse opal nanoarchitecture for ion/electron transport in the Si-on-Ni anode resulted in a lower interfacial resistance and a higher effective Li ion diffusion coefficient.

Recently, a PS (polystyrene) nanosphere-based template method has been used successfully to fabricate Silicon composite core-shell arrays [64-65]. The fabrication strategy made use of a combination of nanosphere lithography and ICP (inductive coupled plasma) dry etching technology to prepare the silicon nanorods array on a silicon wafer substrate. Then, the shell

is deposited by radio frequency (RF) magnetron sputtering; the protective shell on the inner Si core was in one case SnO_2 [64] and in the other case Germanium [65]. The common idea in these two works is to inhibit the pulverization of Si which takes place during cycling due to its large volume expansion, by coating Si with another anode material and at the same time to provide a stable connection with the current collector. The effects of cycling on the core shell structure Si/SnO_2 were studied by post-mortem SEM analysis (see Figure 15), that revealed the beneficial effect of both the bottle like structure and the SnO_2 shell [64]. The Si/SnO_2 nanorods composite still exhibited a good verticality after 100 cycles (see Figure 15a and e) with only small agglomerated areas and few wrinkles on the sidewall of the nanorods (see Figure 15b and f). On the contrary, uncovered Si nanorods displayed cracks in the majority of areas (Figure 15 c, g and h) while a planar Si/SnO_2 electrode after 100 cycles exhibited many areas of aggregation. Thus, the comparison of the morphology of the three different electrodes after cycling definitely proved the beneficial role of the 3D architecture and of the protective shell that could buffer the strain from the volume change during the cycling process.

Previously, a 3D solid state interpenetrating cell was fabricated by filling the available macropore space in a 3DOM carbon anode [66]. The carbon anode was obtained by using monolithic PMMA (polymethyl methacrylate) as colloidal crystal template and resorcinol-formaldehyde polymer as the source of active carbon. Then PPO poly(phenylene oxide) was electrodeposited on the negative electrode and the coated electrode was immersed multiple times in 1M $LiClO_4$/acetonitrile solution to introduce Li^+ to the polymer film. The carbon anode was pre-lithiated and then infiltrated with a V_2O_5 ambigel cathode (see Figure 16). The prototype cell was cycled at current 10-20 μA and a pseudocapacitive voltage profile was observed due to the low ionic conductivity of the V_2O_5 cathode which limited the diffusion of Li^+ ions.

3.2.2 Template-free synthesis of 3D nanoarrays

Self-supported nanostructured arrays for microbatteries have been produced recently without the need of any template, by using the hydrothermal synthesis.

A 3D $Ni/SnO_x/C$ hybrid array was built directly on current collectors via hydrothermal method followed by a reduction/calcination process [67]. A $SnO_2/Ni_2(OH)_2CO_3$ network precursor was grown on stainless steel substrates and then heated at 480°C with a reduction agent (glucose) to reduce Ni^{2+} to Ni. Nanorods of SnO_2 200 nm in length were obtained, showing a rough surface due to the presence of nanoparticles of about 20 nm. The 3D hybrid

nanostructured arrays were used as prepared in a Li cell, exhibiting a maximum areal capacity of 1.75 mAh cm^{-2} (0.1 mA cm^{-2}current rate) and a sufficiently good rate capability, with 0.11 mAh cm^{-2} areal capacity retained when charged in 33 sec at 2.8 mA cm^{-2} current rate.

The hydrothermal synthesis was also used to synthesize crystalline $H_2Ti_2O_5$, $H_2Ti_8O_{17}$, TiO_2-B and anatase TiO_2/TiO_2-B nanowires on a flexible Ti foil [68], aiming at exploring the application of this hydrogen titanium oxide as a new class of anode materials for LIBs and MILBs. Among the tested electrodes, the one based on the single crystalline $H_2Ti_8O_{17}$ nanowire array achieved a discharge capacity greater than 160 mAh g^{-1} and showed at 10C a capacity retention around 95% of the initial discharge capacity.

In the attempt to improve the electrochemical performance of TiO_2 (theoretical capacity 335 mAh g^{-1}) for practical applications, hierarchical TiO_2-B nanowire@a-Fe_2O_3 nanothorn core-branch arrays have been recently prepared by a stepwise hydrothermal approach [69]. Fe_2O_3 was chosen to cover the TiO_2 nanowires due to its high theoretical capacity of about 1000 mAh g^{-1} that could contribute significantly to increase the overall capacity of the hybrid structure. The TiO_2 nanowire arrays appeared like a honeycomb micropattern (see Figure 17a) and this morphology was retained after that Fe_2O_3 was deposited on it. The high magnification SEM images of the TiO_2@a-Fe_2O_3 hybrid array showed Fe_2O_3 nanothorns vertically aligned on the TiO_2 nanowire, forming branches on the TiO_2 nanowire backbones (see Figure 17). The TiO_2@a-Fe_2O_3 electrode could deliver an initial capacity of about 800 mAh g^{-1} (Figure 17 g) which was almost the double of the initial capacity of the TiO_2 based array. In addition to the high gravimetric capacity, the areal capacity of the hybrid array was also remarkable (750 μAh cm^{-2}). EIS spectra demonstrated that the charge transfer resistance of the hybrid array electrode after 50 cycles was lower than the initial one, likely due to an improvement of the electrical conductivity for the formation of Fe particles for the conversion reaction of Fe_2O_3. The fast charge transport between the electrode and the electrolyte was also facilitated by the nanoarchitecture of the electrode owing to the reduced diffusion paths for electrons and lithium ions.

There are very few reports about the preparation of 3D self-standing arrays of positive electrodes [57] and a latest one is dealing with a two-step hydrothermal synthesis of $LiCoO_2$ nanowire arrays on Ti and Au foils [70]. In this work both LT (cubic structure) and HT-$LiCoO_2$ (hexagonal structure) were synthesized and their electrochemical properties were tested in half cells. A marked difference in performance, as expected, was observed for the two electrodes with the HT-$LiCoO_2$ showing better results due to its superior structural

stability. A high reversible capacity of about 103 mAh g^{-1} was achieved by this electrode at 10C rate.

3.2.3 Alternative approaches

In addition to the electrodes and cell designs discussed above, other configurations were developed to optimize the fabrication process and the power/capacity of the MLIBs. Some of them made used of solid electrolytes [71-74].

In particular, a fundamental research carried on at the nanoscale dimension, tried to clarify the scaling limit of a solid electrolyte for an optimal design of miniaturized 3D-MLIBs [74]. The authors of this work fabricated a complete nanobattery (0.5-1 μm in diameter) depositing sequentially the various battery components on Si nanowires, using PVD. The final battery NWLIB (nanowire LIB) constituted by $LiCoO_2$ cathode (Ti/Pt/Ti current collector), LiPON solid electrolyte and n-doped amorphous silicon anode, had a core-multishell geometry (see Figure 18). These NWLIBs were a perfect platform for *in situ* electrochemical experiments compatible with TEM, STEM and FESEM to investigate the structural changes that accompany charge transfer. A CCC-OCP (constant current charging-open circuit potential) constant current discharge protocol was adopted for NWLIBs having a 110 nm and 180 nm thick solid electrolyte layer. A thin film LIB with 360 nm thick LiPON was also prepared and tested. A rapid self-discharge was observed for the nanobattery with the thinnest electrolyte, and in situ TEM revealed the formation of voids along the $LiCoO_2$/LiPON boundary that expanded during cycling. The authors demonstrated that the thickness of the electrolyte should not be smaller than 1 μm otherwise its ability to prevent electronic current flow between anode and cathode might be compromised due to the space-charge limited electronic conduction [74].

The use of a solid electrolyte is highly desirable in microbatteries to avoid leakage problems which could worsen both the operation and the safety of the microdevice powered by the MLIB. Work in this field is still limited, even for thin film batteries [(75) and reference therein]. Some works reported about 3D-MLIBs having a polymer electrolyte [42, 71-72, 76], focusing on the coating approach to obtain a thin conformal coating of the 3D electrodes. The template synthesis of the nanostructured electrodes is in common among these works which instead applied different methods for the deposition of the polymeric film: in situ UV-induced photo-polymerisation [72, 76], hard template assisted drop coating technique [71] and electropolymerization [42]. Good results were shown for a Ni-Sn/PMMA hybrid assembly obtained by drop coating the PMMA gel polymer electrolyte onto Ni-Sn nanowires, after a

pore widening process of the AAO template in which the nanowires were grown [71]. Conformally coated Ni-Sn nanowires showed a reversible capacity of 0.2 mAh cm^{-2} at 3C current rate, with a substantial improvement with respect to an uncoated electrode cycled in a liquid electrolyte.

A ceramic solid state electrolyte $Li_{0.55}La_{0.35}TiO_3$ (LLT) with honeycomb structure was employed to fabricate cells by impregnating a mixture of active material sols into the honeycomb holes [73]. $LiMn_2O_4$ and $Li_4Mn_5O_{12}$ were used as cathode and anode respectively, and the influence of the composition of the precursor sol on the performance of half cells was initially investigated. The full cell was made of a LLT full honeycomb structure with 200 holes on each side of it and a gap between the holes of 80 μm. Both the active materials were well distributed in the honeycomb holes and well in contact with the solid electrolyte. The operational voltage of the cell was 1.2V and a discharge capacity of 32 mAh cm^{-2} was obtained for the first cycle.

Another approach aimed at increasing the cell capacity using a polymer wall to build 3D electrodes on a flat SiO_2/Si substrate on which interdigitated gold current collectors were patterned [77]. $Li_4Ti_5O_{12}$ and $LiCoO_2$ were used as anode and cathode materials to prepare slurries with acetylene black, carboxymethylcellulose and styrene-butadiene rubber. The slurries were injected into the space on the target current collector with the polymer wall as a support. Then, the polymer wall was removed by immersing the electrodes into acetone and a precursor solution of a gel polymer electrolyte based on PMMA was filled into the vacancies of anode and cathode and thermally polymerized to obtain the full 3D-MLIB. The cell was cycled and showed a reversible behaviour, delivering a discharge capacity of about 270 μAh cm^{-2} at 2C rate with a potential plateaus at 2.35V during both the charge and the discharge of the cell [77].

A completely different and original methodology was used to fabricate a fully packaged ultrahigh energy density microbattery [78] using densely sintered electrodes. The idea at the basis of this work is that sintered intercalation oxides with appropriate 3D pore topologies could provide electrodes with superior energy densities. The authors demonstrated that $LiCoO_2$ with a density between 65-85% of the theoretical crystal density can be cycled repeatedly to the theoretical capacity limit without evidence of material disintegration. Taking advantage of the semiconductor to metal transition of the partially delithiated $Li_{1-x}CoO_2$ ($x > 0.06$) for which a significant increase in conductivity is observed ($> 10^{-3}$ S cm^{-1}) no conductive additives were used in the electrode, as well as no binders were needed. After the assessment of the electrodes performance, a 6 mm^3 volume microbattery based on $LiCoO_2$/Li chemistry

was sealed with an electroformed packaging (see Figure 19 a and b). The microbatteries were subjected to charge/discharge and impedance tests. Cells charged to voltages of 4.5 and 4.6V exhibited discharge energy densities > 350 WhL^{-1} at power densities exceeding 150 WL^{-1} and energy of 650 WhL^{-1} at 200 WL^{-1} power, respectively (see Figure 19c). The energy densities achieved by this microbattery were previously obtained only at cell volumes more than 100 times larger.

An attempt has also been made to practically investigate the aperiodic aerogel-like architectures in order to gain information on the electrical response and ionic transport of a tricontinuous sponge geometry (see Figure 20a) [79]. A self-wired 3D charge-insertion scaffold was at first obtained by synthesizing a MnO_x ultraporous ambigel positive electrode directly on an ITO current collector and then by electrodepositing an ultrathin polymer separator (polyphenylene oxide PPO) on it. This later step was particularly crucial since a conformal, pinhole free polymer separator is needed, but attention had to be paid to avoid clogging the pores of the ambigel network. In fact, the remaining 3D interconnected nanoscopic void volume might be infused with a melt metal of some relevance for LIBs (i.e. In or Li) or as in this case by a nanostructured oxide such as RuO_2. The authors demonstrated through TEM images the architectural integration of the components necessary to build a battery and the tricountinous design of this porous structure (Figure 20 b). Lithiated samples ITO‖Li_xMnO_x‖PPO and full solid-state cells ITO‖Li_xMnO_x‖PPO‖RuO_2‖Ga-In were also prepared. The full cells exhibited a zero open-circuit potential to explain which different hypothesis were taken into account: i) electrical short, ii) not enough Li ions into the polymer layer, iii) presence of pinholes in the ultrathin PPO, iv) a soft short caused by a change in the electrical properties of PPO due to the deposition of RuO_2 [79]. This work has clearly demonstrated that notwithstanding some benefits of the sponge design great efforts are still needed to make the fabrication process easier and effective.

4 – Future directions

4.1- Laser structuring and 3D printing

Although numerous designs and fabrication methodologies have been proven efficient to prepare 3D-MLIBs, there is still a lack of a simple and economic strategy to construct the 3D architectured electrodes.

Laser structuring is a technique currently used to modify by ablation the surface and the shape of many industrially relevant products (silicon wafers for solar cells, coating on glass for photovoltaic panels, patterning of plastic injection tools etc.). In recent years, this method has

been applied to obtain 3D nanostructured electrodes for microbatteries, starting from thin or thick films and from conventional tape-cast electrodes. In particular the self-organization of microstructures by irradiation with a homogeneous laser beam has been the focus of some work [80-82]. $LiCoO_2$ thin films deposited by r.f. magnetron sputtering showed the formation of conical surface structures after irradiation with a laser beam (see Figure 21a) [83]. The laser parameters such as the laser fluence have a significant impact on the formation of these self-organized structures, that still remain a not completely understood phenomenon [80]. Interestingly, it was demonstrated that a very similar kind of surface structure can be obtained also on tape cast electrodes of $LiCoO_2$ conventionally prepared with a binder and carbon black (see Figure 21b) [80]. Self-organized structures with height of about 20 μm were formed, and the SEM of cross sections of the conical structures revealed the presence of the additives inside the conical structure (see Figure 21c). The effect on the electrochemical performance is an improved cycling stability at higher current rates of the laser structured $LiCoO_2$ electrode.

Direct writing denotes a group of techniques used to precisely deposit a variety of materials onto a substrate in digitally defined locations [84] and among them inkjet printing, laser printing and in general all the layered-based methods have shown remarkable potential for the fabrication of modern products. The application of these techniques to the fabrication of MLIBs requires the development of ink-like mixtures of the electrode materials with proper colloidal properties in order to make them compatible with the printing machines.

Some years ago the laser direct-write was demonstrated to be a valuable tool to fabricate micropower sources [20, 85] such as primary Zn-Ag_2O and secondary lithium cells. Zn anodes and Ag_2O cathodes were deposited in a planar configuration, while a stacked geometry was chosen for the Li cell, in which $LiMn_2O_4$ and carbon were the cathode and the anode active materials respectively [20]. For the lithium cell, 3mm x 3mm pockets were laser machined into polyimide sheets and backed with Al and Cu foil that acted as current collectors. Inks of the active materials were at first deposited on a boron silicate glass then irradiated through the back with a Nd:YVO_4 laser (λ=355nm) to transfer the material into the polyimide pockets. The polymer separator was deposited by drop casting over each electrode and the microbattery was assembled by stacking the cathodic pocket over the anodic one. The open circuit voltage of the cell was 3.8V and the cell could be charged and discharged for 50 cycles showing a capacity of about 110 μAh cm^{-2} [20]. This cell had no packaging and was operated entirely inside a glove box. In the following years a zinc-silver microbattery was developed again by

using a custom made super ink-jet printing system, but using arrays of silver pillars to obtain a 3D configuration [86].

The laser direct write technique was also used recently to manufacture porous composite cathodes containing active materials, binder and carbon black and in combination with laser structuring in order to form 3D structured electrodes [81-82]. A detailed study was done to investigate the performance of laser printed $LiMn_2O_4$ thick films used as prepared or after calendering, or after laser structuring, and structuring and calendering (see Figure 22, flow chart and SEM images) [81]. The advantages of using calendered electrodes is well known in case of conventional bulk batteries, for which a better electrical contact and a homogeneous film thickness together with a controlled porosity achieved through calendering of the electrodes, in general enables to increase the energy (and power) density. Pröll et al. studied the impact of calendering and of its combination with laser structuring on the electrochemical performance of 3D microstructured electrodes. SEM pictures of the laser-printed thick film (Figure 22 b) and c)) showed the interconnection among $LiMn_2O_4$ particles and the homogeneous distribution of the carbon black and binder. After femtosecond fs-laser structuring both the un-calendered and calendered films had a 3D grid microstructure (Figure 22 d) and e)) and the mass loss after structuring was measured to be 13-15 wt% for uncalendered and 16-17% for calendered samples. The electrodes were then subjected to electrochemical formation by using CV measurements, then to C-rate testing and after the galvanostatic measurements the cell kinetics and reversibility was assessed by means of CV measurements. The authors found that the laser structuring process increased Li-ion diffusion kinetics; the calendered/structured films showed the highest peak currents and could retain about 70% of their initial discharge capacity at 1C rate, exhibiting less degradation (see Figure 22a). The overall improvement of cycling performance of the calendered/laser structured cathode was attributed to the combination of increased electrical contact and shortened Li-ion migration pathways.

The ability to print a separator/electrolyte would be of high importance for the development of all-solid-state 3D printed MLIBs. So far, very few information is available on polymer printing in the field of microbatteries, probably due to some limitations related to the low viscosity requirements of the jetting process. The feasibility of a polymer ink-jet printing technique for the construction of 3D micro-patterned structures was systematically investigated, but without any specific application in mind [87]. The laser-direct write printing process was used to fabricate a ceramic-solid polymer ionic liquid nanocomposite, a $LiCoO_2$ cathode and a carbon anode to obtain a complete microbattery after sequentially stacking all

the components [88]. The main focus of this work was the preparation of the laser transferable polymer gel separator formulated from an imidazolium-based ionic liquid, PVDF-HFP and TiO_2 nanopowder (to enhance the mechanical strength and partially absorb the incident laser radiation). The gel electrolyte showed a very good conductivity at ambient temperature (2-3 mS cm^{-1}), greater than for LIPON and other amorphous polymers. Recently, a work has been published demonstrating the ink-jet printing of an ionogel proposed as a solid electrolyte for MLIBs [89]. The sol precursor of the ionogel was prepared by mixing tetramethyl orthosilicate (TMOS), the ionic liquid N-methyl-N-propylpyrrolidinium bis(trifluoromethan)suflonylimide (PYR_{13}-TFSI) and the Li salt lithium bis(trifluoromethan)sulfonylimide (LiTFSI). The viscosity of the ionogel precursor was low enough for printing (approximately 10 mPa s) and the deposition was directly performed onto the porous composite electrodes ($LiFePO_4$ and $Li_4Ti_5O_{12}$ cathode and anode active materials respectively). Half cells and complete cells were tested; a surface capacity of 300 μAh cm^{-2} was delivered for the full cell, corresponding to a specific capacity of 60 $mAhg^{-1}$ for the $LiFePO_4$ electrode.

An innovative, economic and fast approach was recently proposed that drew the attention on the application of additive layer manufacturing to the fabrication of interdigitated 3D microbattery architecture 3D-IMA [7]. Although the 3D printing technique is quite simple, the optimization of the composition and rheology of the inks was of crucial importance to prevent clogging of the nozzles of the print head, to promote adhesion between the printed features and to provide structural integrity. $Li_4Ti_5O_{12}$ (LTO) and $LiFePO_4$ (LFP) were chosen as active materials for the anode and the cathode, respectively. The inks were printed on an interdigitated gold current collector previously patterned on a glass substrate by a combination of lithographic patterning and e-beam deposition (see the schematic illustration of Figure 23a). After printing the structures were annealed at 600°C (Figure 23b) and then a PMMA preform was laser cut, placed around the microbattery, filled with a standard liquid electrolyte (1M $LiClO_4$ 1:1 EC:DMC) and sealed (Figure 23c). At first, the discharge properties of half cells were measured comparing in particular the behaviour of 8-layer and 16-layer structures. A non-monotonic variation of the discharge capacity with the number of layers (volume) was observed, thus indicating that the height of the structure can negatively affect the electronic transport and the kinetics of the reaction. A complete battery composed by 8-layer LTO-LFP was then cycled at different C rates and showed a stable working voltage of 1.8V when discharged below 5C rate (see Figure 23d). The capacity of the packaged 3D-IMA was 1.2 mAh cm^{-2} but the packaging needed to be optimized due to lack of hermeticity that inhibited

the long cycling of the cell. Anyway, the unpackaged full cell demonstrated an areal energy density as high as 9.7 J cm^{-2} at a power density 2.7 mW cm^{-2} and could potentially find application in autonomously powered microdevices.

4.2-A promising anode material: Silicon.

Si is one of the anode materials of choice for next generation Li-ion batteries due to its high specific capacity (energy density) of 3579mAh/g for $Li_{3.75}Si$. Additional considerations as to why it is a preferential material are that Si is the second most abundant element in the earth's crust and is also environmentally benign. Unfortunately, at full lithiation a Si particle expands by 270% and this presents significant structural stability challenges at the level of the entire electrode. During lithiation, Si particles expand and encroach on each other and during delithiation, Si particles contract, which can result in detachment from surrounding electrical connections [90]. Such a drastic electrode morphology change can further contribute to capacity fading. In addition, the total volume of the whole Si anode also increases and decreases upon lithiation and delithiation and this will lead to electrode delamination and failure. Si is also unstable with the carbonate organic electrolytes, forming a non-stable solid-electrolyte interphase (SEI). This occurs when the electrolyte undergoes reductive decomposition during lithiation because the operating potential of Si is below 0.5V (vs Li), which is beyond the lowest unoccupied molecular orbital (LUMO) of the carbonate electrolytes (*ca.* 1.3V).

To circumvent volume expansion issues, various Si nano-structuring approaches have been investigated as a means to generate optimal electrode architectures, with many of these incorporating nanowire [91-92] nanoparticle [93-96] or hollow Si nanoparticles [97] or nanotubes [98].

Very recently, composite Si – C microbatteries have also been investigated by Biserni *et al* [99] using two novel approaches, one of those based on the deposition of nanostructured porous amorphous Si films by PLD at room temperature on a foil made of carbon nanotubes. Within these anode films nano-scale voids are introduced to help accommodate the volume expansion and areal capacities of 175µAh/cm were exhibited. Carbon nanotubes acted as current collectors, so that the standard copper collector was unnecessary. Therefore, the thickness of the overall electrode was significantly reduced, thus addressing the requirements for application in innovative microbatteries.

There is considerable scope for further developments around Si and Si-composite anode inks, especially with a view to using a "sprinkling" strategy by adding % of Si materials to

incrementally increase capacity in carbon-based anodes. Increasing our understanding of failure modes in Si electrodes and how to overcome these by re-engineering materials or electrodes will facilitate further advances in these technologies. Particular consideration to the electrode architecture and anode and cathode configuration is key to performance in microbatteries.

5 – Concluding remarks

MLIBs are critical components for current and next generation devices most of which carry important implications, including healthcare diagnostics, security and component tracking. Several planar MLIB configurations have been tested with only few currently on the market. 3D-MLIBs are an important alternative which have demonstrated an effectively increased energy density by fully utilizing the limited volume available. In particular, the 3D microarchitecture has favoured the exploration of new materials promising for high energy density devices, such as silicon, which benefits from these designs showing a better mechanical integrity.

The manufacturing of 3D structures is far from trivial and can often involve tedious processes including depositions of materials, implying a considerable final cost. Moreover, the integration of a MLIB onto a substrate suffers of some temperature and stability restrictions that drive toward alternative materials and processing selections. Cost saving production technologies are highly desirable and the evaluation of different fabrication approaches such as 3D printing has shown its potential impact also on the field of MLIBs.

Several significant challenges among which the need of an increased shelf life (implying a low self-discharge after years of storage), of a long life cycle, of recharging at high currents and of a volumetrically efficient package design still limit the commercial implementation of the 3D-MLIBs. However, advancements in the research achieved in these last years suggest that a careful design approach and materials choice may take the concept of a 3D-MLIB to a practical application in the near future.

References

1. J. F. M. Oudenhoven, L. Baggetto, P. H. L. Notten, Adv. Energy Mater. 1 (2011) 10.
2. C. C. Ho, J. W. Evans, P. K. Wright, Energy Harvesting of Autonomous Systems, Artech House (2010) 220.
3. http://www.enfucell.com/softbattery; http://www.cymbet.com/products/enerchip-solid-state-batteries.php; http://www.solicore.com/
4. S. J. Dillon, K. Sun, Curr. Opinion Solid State Mat. Sci. 16 (2012) 153.
5. R. Salot, S. Martin, S. Oukassi, M. Bedjaoui, J. Ubrig, Appl. Surf. Sci. 256S (2009) S54.
6. J. H. Pikul, H. Gang Zhang, J. Cho, P. V. Braun, W. P. King, Nat. Comm. 4 (2013) 1732.
7. K. Sun, T.-S. Wei, B. Y. Ahn, J. Y. Seo, S. J. Dillon, J. A. Lewis, Adv. Mater. 25 (2013) 4539.
8. T. S. Arthur, D. J. Bates, N. Cirigliano, D. C. Johnson, P. Malati, J. M. Mosby, E. Perre, M. T. Rawls, A. L. Prieto, B. Dunn, Mat. Res. Bull. 36 (2011) 523.
9. M. Roberts, P. Johns, J. Owen, D. Brandell, K. Edstrom, G. El Enany, C. Guery, D. Golodnitsky, M. Lacey, C. Lecoeur, H. Mazor, E. Peled, E. Perre, M. M. Shaijumon, P. Simon, Pierre-Louis Taberna, J. Mater. Chem. 21 (2011) 9876.
10. K. Edstrom, D. Brandell, T. Gustafsson, L. Nyholm, Interface, 20 (2011) 41.
11. B. Y. Ahn, E. B. Duoss, M. J. Motala, X. Guo, S.-I. Park, Y. Xiong, J. Yoon, R. G. Nuzzo, J. A. Rogers, J. A. Lewis, Science 323 (2009) 1590.
12. B. C. Gross, J. L. Erkal, S. Y. Lockwood, C. Chen, D. M. Spence, Anal. Chem. 86 (2014) 3240.
13. R. W. Hart, H. S. White, B. Dunn, D. R. Rolison, Electrochem. Commun. 5 (2003) 120.
14. V. Zadin, D. Brandell, H. Kasemägi, J. Lellep, A. Aabloo, J. Power Sources 244 (2013) 417.
15. V. Zadin, H. Kasemägi, A. Aabloo, D. Brandell, J. Power Sources 195 (2010) 6218.
16. D. G. Lim, D.-W. Chung, R. Kohler, J. Proell, C. Scherr, W. Pfleging, R. E. Garcia, J. Electrochem. Soc. 161 (2014) A302.
17. G. Nagasubramanian, D. H. Doughty, J. Power Sources 136 (2004) 395.
18. B. Fleutot, B. Pecquenard, F. Le Cras, B. Delis, H. Martinez, L. Dupont, D. Guy-Bouyssou, J. Power Sources 196 (2011) 10289.
19. Y.-N. Zhou, M.-Z. Xue, Z.-W. Fu, J. Power Sources 234 (2013) 310.
20. A. Pique´, C. B. Arnold, H. Kim, M. Ollinger, T. E. Sutto, Appl. Phys. A 79 (2004) 783.
21. H. Kim, R. C. Y. Auyeung, A. Pique´, J. Power Sources 165 (2007) 413.
22. H. Nakano, K. Dokko, J. Sugaya, T. Yasukawa,T. Matsue, K. Kanamura, Electrochem. Comm. 9 (2007) 2013.

23. F. Albano, Y.S. Lin, D. Blaauw, D. M. Sylvester, K. D. Wise, A. M. Sastry, J. Power Sources 185 (2008) 1524.
24. K. Marquardt, R. Hahn, M. Blechert, M. Lehmann, M. Töpper, M. Wilke, P. Semionyk, M. von Suchodoletz, H. Reichl, Microsyst Technol 16 (2010) 1119.
25. K. Marquardt, R. Hahn, T. Luger, H. Reichl, MEMS (2006) Istanbul, Turkey, 954.
26. R. Hahn, K. Höppner, K. Marquardt, M. Eisenreich, M. Ferch, M. Wilke, K.-D. Lang, IEEE (2012) 619.
27. K. Hoeppner, M. Ferch, M. Eisenreich, K. Marquardt, R. Hahn, P. Mackowiak, B. Mukhopadhyay, H.-D. Ngo, R. Gernhardt, M. Toepper, K.-D. Lang, J. Physics: Conference Series 476 (2013) 012086.
28. D. R. Rolison, J. W. Long, J. C. Lytle, A. E. Fischer, C. P. Rhodes, T. M. McEvoy, M. E. Bourg, A. M. Lubers, Chem. Soc. Rev. 38 (2009) 226.
29. J. W. Long, B. Dunn, D. R. Rolison, H. S. White, Chem. Rev. 104 (2004) 4463.
30. P. H. L. Notten, F. Roozeboom, R. a. H. Niessen, L. Baggetto, Adv. Mater. 19 (2007) 4564.
31. L. Baggetto, R. A. H. Niessen, F. Roozeboom, P. H. L. Notten, Adv. Funct. Mater. 18 (2008) 1057.
32. G. Oltean, L. Nyholm, K. Edström, Electrochimica Acta 56 (2011) 3203.
33. P. L. Taberna, S. Mitra, P. Poizot, P. Simon, J.-M. Tarascon, Nat. Materials 5 (2006) 567.
34. Y. Lei, B. Daffos, P.L. Taberna, P. Simon, F. Favier, Electrochimica Acta 55 (2010) 7454.
35. C. Lecoeur, J.-M. Tarascon, C. Guery, J. Electrochem. Soc. 157 (2010) A641.
36. S. R. Gowda, A. L. M. Reddy, X. Zhan, H. R. Jafry, P. M. Ajayan, Nano Lett. 12 (2012) 1198.
37. X. Chen, K. Gerasopoulos, J. Guo, A. Brown, C. Wang, R. Ghodssi, J. N. Culver, ACSNano, 4 (2010) 5366.
38. Y. Liu, W. Zhang, Y. Zhu, Y. Luo, Y. Xu, A. Brown, J. N. Culver, C. A. Lundgren, K. Xu, Y. Wang, C. Wang, Nano Lett. 13 (2013) 293.
39. K. Gerasopoulos, M. McCarthy, E. Royston, J. N. Culver, R. Ghodssi, J. Micromech. Microeng. 18 (2008) 104003.
40. C. Wang, G. Jia, L. H. Taherabadi, M. J. Madou, J. Microelectromech. Syst. 14 (2005) 348.
41. H.-S. Min, B. Y. Park, L. Taherabadi, C. Wang, Y. Yeh, Rabih Zaouk, M. J. Madou, B. Dunn, J. Power Sources 178 (2008) 795.
42. M. Valvo, M. Roberts, G. Oltean, B. Sun, D. Rehnlund, D. Brandell, L. Nyholm, T. Gustafsson, K. Edström, J. Mater. Chem. A 1 (2013), 9281.
43. P. Johns, M. Roberts, J. Owen, J. Mater. Chem. 21 (2011) 10153.

44. M. Nathan, D. Golodnitsky, V. Yufit, E. Strauss, T. Ripenbein, I. Shechtman, S. Menkin, E. Peled, J. Microelectr. Syst. 14 (2005) 879.
45. D. Golodnitsky, V. Yufit, M. Nathan, I. Shechtman, T. Ripenbein, E. Strauss, S. Menkin, E. Peled, J. Power Sources 153 (2006) 281.
46. D. Golodnitsky, M. Nathan, V. Yufit, E. Strauss, K. Freedman, L. Burstein, A. Gladkich, E. Peled, Solid State Ionics 177 (2006) 2811.
47. H. Mazor, D. Golodnitsky, L. Burstein, E. Peled, Electrochem. Solid State Lett. 12 (2009) A232.
48. E. Eustache, P. Tilmant, L. Morgenroth, P. Roussel, G. Patriarche, D. Troadec, N. Rolland, T. Brousse, C. Lethien, Adv. Energy Mater. 4 (2014) 1301612.
49. F. Chamran, Y. Yeh, H.-S. Min, B. Dunn, C.-J. Kim, J. Microelectromech. Syst. 16 (2007) 844.
50. G. Turon Teixidor, R. B. Zaouk, B. Y. Park, M. J. Madou, J. Power Sources 183 (2008) 730.
51. N. Cirigliano, G. Sun, D. Membreno, P. Malati, C. J. Kim, B. Dunn, Energy Technol. 2 (2014) 362.
52. W. Lee, S.-J. Park, Chem. Rev. 114 (2014) 7487.
53. S. K. Cheah, E. Perre, M. Rooth, M. Fondell, A. Hårsta, L. Nyholm, M. Boman, T. Gustafsson, J. Lu, P. Simon, K. Edström, Nano Lett., 9 (2009) 3230.
54. M. Valvo, D. Rehnlund, U. Lafont, M. Hahlin, K. Edström, L. Nyholm, J. Mater. Chem. A 2 (2014) 9574.
55. W. Wang, M. Tian, A. Abdulagatov, S. M. George, Y.-C. Lee, R. Yang, Nano Lett. 12 (2012) 655.
56. X. Wu, S. Zhang, H. Fang, Z. Du, R. Lin, J. Power Sources 264 (2014) 311.
57. M. M. Shaijumon, E. Perre, B. Daffos, P. L. Taberna, J.-M. Tarascon, P. Simon, Adv. Mater. 22 (2010) 4978.
58. N. Li, C. R. Martin, J. Electrochem. Soc. 148 (2001) A164.
59. K. Gerasopoulos, E. Pomerantseva, M. McCarthy, A. Brown, C. Wang, J. Culver, R. Ghodssi, ACSNano 6 (2012) 6422.
60. Y. Liu, W. Zhang, Y. Zhu, Y. Luo, Y. Xu, A. Brown, J. N. Culver, C. A. Lundgren, K. Xu, Y. Wang, C. Wang, Nano Lett. 13 (2013) 293.
61. S.-W. Kim, T. H. Han, J. Kim, H. Gwon, H.-S. Moon, S.-W. Kang, S. O. Kim, K. Kang, ACSNano 3 (2009) 1085.
62. A. Stein, B. E. Wilson, S. G. Rudisill, Chem. Soc. Rev. 42 (2013) 2763.
63. H. Liu, H.-M. Cho, Y. S. Meng, Q. Li, ACS Appl. Mater. Interfaces 6 (2014) 9842.

64. C. Yue, Y. Yu, J. Yin, T. Wong, Y. Zang, J. Li, J. Kanga, J. Mater. Chem. A 1 (2013) 7896.
65. Y. Yu, C. Yue, S. Sun, W. Lin, H. Su, B. Xu, J. Li, S. Wu, J. Li, J. Kang, ACS Appl. Mater. Interfaces 6 (2014) 5884.
66. N. S. Ergang, M. A. Fierke, Z. Wang, W. H. Smyrl, A. Stein, J. Electrochem. Soc. 154 (2007) A1135.
67. J. Zhu, J. Jiang, Y. Feng, G. Meng, H. Ding, X. Huang, ACS Appl. Mater. Interfaces 5 (2013) 2634.
68. J.-Y. Liao, X. Xiao, D. Higgins, G. Lui, Z. Chen, ACS Appl. Mater. Interfaces 6 (2014) 568.
69. H. Xia, W. Xiong, C. Keat Lim, Q. Yao, Y. Wang, J. Xie, Nano Res. 7 (2014) 1797.
70. H. Xia, Y. Wan, W. Assenmacher, W. Mader, G. Yuan, L. Lu, NPG Asia Materials 6 (2014) e126.
71. S. R. Gowda, A. L. Mohana Reddy, M. M. Shaijumon, X. Zhan, L. Ci, P. M. Ajayan, Nano Lett. 11 (2011) 101.
72. S. Tan, E. Perre, T. Gustafsson, D. Brandell, Solid State Ionics 225 (2012) 510.
73. M. Kotobuki, Y. Suzuki, H. Munakata, K. Kanamura, Y. Sato, K. Yamamoto, T. Yoshida, Electrochimica Acta 56 (2011) 1023.
74. D. Ruzmetov, V. P. Oleshko, P. M. Haney, H. J. Lezec, K. Karki, K. H. Baloch, A. K. Agrawal, A. V. Davydov, S. Krylyuk, Y. Liu, J. Y. Huang, M. Tanase, J. Cumings, A. A. Talin, Nano Lett. 12 (2012) 505.
75. C. Gerbaldi, M. Destro, Jijeesh R. Nair, S. Ferrari, I. Quinzeni, E. Quartarone, Nano Energy 2 (2013) 1279.
76. S. Tan, S. Walus, J. Hilborn, T. Gustafsson, D. Brandell, Electrochem. Comm. 12 (2010) 1498.
77. K. Yoshima, H. Munakata, K. Kanamura, J. Power Sources 208 (2012) 404.
78. W. Lai, C. K. Erdonmez, T. F. Marinis, C. K. Bjune, N. J. Dudney, F. Xu, R. Wartena, Y.-M. Chiang, Adv. Mater. 22 (2010) E139.
79. C. P. Rhodes, J. W. Long, K. A. Pettigrew, R. M. Stroud, D. R. Rolison, Nanoscale 3 (2011) 1731.
80. R. Kohler, J. Proell, M. Bruns, S. Ulrich, H.J. Seifert, W. Pfleging, Appl Phys A 112 (2013) 77.
81. J. Pröll, H. Kim, A. Piqué, H.J. Seifert, W. Pfleging, J. Power Sources 255 (2014) 116.
82. H. Kim, J. Proell, R. Kohler, W. Pfleging, A. Pique, J. Laser Micro/Nanoeng. 7 (2012) 320.
83. R. Kohler, P. Smyrek, S. Ulrich, M. Bruns, V. Trouillet, W. Pfleging, J. Optoelectron.. Adv. Mater. 12 (2010) 547.

84. K.K.B. Hon, L. Li, I.M. Hutchings, CIRP Annals - Manufacturing Technology 57 (2008) 601–620.
85. R. Wartena, A. E. Curtright, C. B. Arnold, A. Piqué, K. E. Swider-Lyons, J. Power Sources 126 (2004) 193.
86. C. C. Ho, K. Murata, D. A. Steingart, J. W. Evans, P. K. Wright, J. Micromech. Microeng. 19 (2009) 094013.
87. Y. H. Yun, J. D. Kim, B. K. Lee, Y. W. Cho, H. Y. Lee, Macromolecular Res. 17 (2009) 197.
88. T. E. Sutto, M. Ollinger, H. Kim, C. B. Arnold, A. Piqué, Electrochem. Solid-State Lett. 9 (2006) A69.
89. P.-E. Delannoy, B. Riou, B. Lestriez, D. Guyomard, T. Brousse, J. Le Bideau, J. Power Sources 274 (2015) 1085.
90. B. Liang, Y. Liu, Y. Xu, J. Power Sources 267 (2014) 469.
91. C. K. Chan, H. Peng, G. Liu, K. McIlwrath, X. F. Zhang, R. A. Huggins, Y. Cui, Nature Nanotech. 3 (2008) 31.
92. L.-F. Cui, R. Ruffo, C. K. Chan, H. Peng, Y. Cui, Nano Lett. 9 (2009) 491.
93. M. T. McDowell, S. W. Lee, I. Ryu, H. Wu, W. D. Nix, J. W. Choi, Y. Cui, Nano Lett. 11 (2011) 4018.
94. X. Zhou, Y.-X. Yin, A.-M. Cao, L.-J. Wan, Y.-G. Guo, ACS Appl. Mater. Interfaces 4 (2012) 2824.
95. L.-F. Cui, L. Hu, H. Wu, J. W. Choi, Y. Cui J. Electrochem Soc, 158 (2011) A592.
96. L. Hu, H. Wu, S. S. Hong, L. Cui, J. R. McDonough, S. Bohy, Y. Cui, Chem. Commun. 47 (2011) 367.
97. H. Ma, F. Cheng, J.-Y. Chen, J.-Z. Zhao, C.-S. Li, Z.-L. Tao, J. Liang, Adv. Mater 19 (2007) 4067.
98. T. Song, H. Cheng, H. Choi, J.-H. Lee, H. Han, D. H. Lee, D. S. Yoo, M.-S. Kwon, J.-M. Choi, S. G. Doo, H. Chang, J. Xiao, Y. Huang, W. I. Park, Y.-C. Chung, H. Kim, J. A. Rogers, U. Paik, ACS Nano 6 (2012) 303.
99. E. Biserni, M. Xie, R. Brescia, A. Scarpellini, M. Hashempour, P. Mohaved, M. Bestetti, A. Li Bassi, P. Bruno, IMLB2014 Villa Erba, Como, Italy, June 10th 2014, MA436.

Tables

Table 1- Dimension, capacity and cell voltage of some commercial MLIBs based on different chemistries.

Company	Anode	Cathode	Dimensions /[cm] (T x H x W)	Capacity /[mAh]	Cell voltage /[V]	Type
EnFilm	Li	$LiCoO_2$	0.02x2.54x2.54	0.7	3.9	Solid state
Solicore	Li	MnO_2	0.045 x ? x ?	10-14	3.0	Li Polymer
Blue Spark	Zn	MnO_2	0.05x7.9x4.7 (max)	10-37	1.5	Primary Battery
Cymbet	n/a	n/a	0.09x0.5x0.5	0.012-0.05	4-4.15	Solid state
Enfucell	Zn	MnO_2	0.07x3.6x4.6	18	1.5	Primary
IPS	Li	n/a	0.02x1.3x1.3	0.13	4.1	Solid state
Exxellatron	Li/Sn_3N_4	$LiCoO_2$	0.037x5x3.8	0.1-10	3.9-4.1	Solid state

Figure Captions

Figure 1- Typical electrical consumption for different mobile devices (taken from ref. [5] with permission from Elsevier)

Figure 2- Representative configuration of a) planar b) stacked microbatteries.

Figure 3 a) Cross-sectional SEM micrograph of a packaged thick film microbattery 1) Cu current collector, (2) carbon anode, (3) GPE soaked separator, (4) $LiCoO_2$ cathode, and (5) Al current collector (taken from ref. [21] with permission from Elsevier; b) Optical microscope images of the substrate for single cell from left to right and from top to bottom: after fabrication of Au current collector by photolithography, after injection of Li–Mn–O sol and Li–Ti–O sol on Au electrode area, after preparation of $LiMn_2O_4$ and $Li_4Ti_5O_{12}$, and after fabrication of MES film on active materials [taken from ref. [22] with permission from Elsevier].

Figure 4- a) Size vs. energy density range comparison of silicon integrated microbattery with existing battery technologies (taken from ref. [26] with permission from IEEE); b) schematic profile of a battery with side-by-side electrode setup (arrows indicate paths of Li-ion movement); c) picture of a chip with two sealed cells (chip size 15x10 mm) (taken from ref. [27] with permission from IOP Publishing).

Figure 5-Different 3D microbatteries architectures: a) interdigitated rod electrodes, b) interdigitated plates or 3D-trench, c) concentric tube design and d) 3D aperiodic sponge [taken from ref. [15] with permission from Elsevier].

Figure 6- a) SEM micrograph of electrodeposited nanorods [taken from ref. [32] with permission from Elsevier]; b) Cross-sectional view of Cu-nanostructured current collector [taken from ref. [33] with permission from Nature Publishing Group]; c) SEM photo of Carbon post arrays after pyrolisis and d) two level C-MEMS electrodes with underneath carbon contacts [taken from ref. [40] with permission from IEEE].

Figure 7- a) Schematic isometric view of the 3D thin film microbattery; b) SEM micrograph of a full 3D-MLIB filled with the graphite anode; c) comparison of the capacity between the battery shown in

a) and a 2D thin film battery based on the same components [taken from ref. [44] with permission from IEEE].

Figure 8- a) Schematic view of a 3D Li-ion microbattery based on a silicon microtube scaffold; b) SEM images of the silicon microtubes with the photoresist acting as the ecthing mask and c) after the photoresist has been stripped away and Pt and TiO_2 have been deposited by ALD [taken from ref. [48] with permission from Wiley].

Figure 9- a) Schematic of the primary steps for 3D carbon post-fabrication and b) 3D carbon arrays with a 3:5:1 aspect ratio [taken from ref. [51] with permission from Wiley].

Figure 10-a) Areal discharging capacity of 32 μm long 3-D Ni/TiO_2 nanowire network and (b) cross-sectional SEM image of 3-D Ni/TiO_2 nanowire network after 72 cycles of battery testing at a discharging rate of ~1.3C [taken from ref. [55] with permission from ACS].

Figure 11- TEM image of a) segmental individual Cu@SnS core-shell nanowire and of b) a segment of an individual SnS/CuS nanotube with open tips formed after completely dissolving the Cu-core (inset shows FFT pattern and TEM image of aligned nanotubes); c) cycling performance of the Cu@SnS electrode (I) and of a SnS layer deposited on a planar Cu foil (II) at different rates [taken from ref. [56] with permission from Elsevier].

Figure 12- a) TEM image of a vertical TMV1cys/Ni/Si nanowire after 45 min of silicon PVD, including EDS profile of Ni and Si and b) cycling performance at 2C current rate [taken from ref. 37 with permission from ACS]; c) schematic description of TMV-templated near-vertical assembly of $LiFePO_4$ nanoforest on current collector with multi-layered nanohierarchical arrangement of active materials and electron conducting pathway and d) rate performance of 3D C/$LiFePO_4$/Ti/Ni, 3D $LiFePO_4$/Ti/Ni nanowire forest cathodes and 2D $LiFePO_4$/Ti thin film cathode at different charge/discharge currents [taken from ref. [60] with permission from ACS].

Figure 13- a) Schematic of the fabrication process where the nickel scaffold defines that the battery architecture and the active materials are electrodeposited onto the nickel scaffold; b) The nanoporous microbattery electrodes consist of an electrolytically active layer (red and yellow) coated on an electrically conductive bicontinuous nickel scaffold (blue). The nickel scaffold acts as the current collector attached to an outside circuit.

c) Scanning electron microscopy (SEM) cross-section of the interdigitated electrodes spanning two periods. The interdigitated electrodes alternate between anode and cathode. The insets show the magnified electrodes with the nickel scaffold coated with nickel–tin on the left and lithiated manganese oxide on the right. Scale bars, 50 mm and 1 mm in the insets. d) A top-down SEM image of the interdigitated electrodes with the anode electrodes connecting at the top, cathode electrodes connecting at the bottom and the interdigitated anode and cathode electrodes overlapping in the middle. Scale bar, 500 μm [taken from ref. [6] with permission from Nature Publishing Group].

Figure 14 - Schematics of the synthetic process of the Si-on-Ni inverse opal electrode. Top view SEM images of the (b) as-deposited (side-view shown in the inset); (c) electropolished Ni inverse opal (EDX of the sample shown in the inset); (d) Si deposited on Ni inverse opal scaffold (EDX of the sample shown in the inset) [taken from ref. [63] with permission from ACS].

Figure 15- SEM images of areas (a) and (b) in Si–SnO_2 NR composite electrode and (c) in Si NRs after Li ion insertion/extraction at a current density of 100 μA cm^{-2} within the voltage window between 0.1 and 2.0 V vs. Li/Li^+ for 100 cycles; and as a comparison (d) area in planar Si–SnO_2 electrode after 100 cycles at a current density of 20 μA cm^{-2} within the voltage window from 0.13 to 2.0 V vs. Li/Li^+; then the corresponding images at higher magnification (e) and (f) from areas of (a) and (b) respectively, (g) and (h) from area of (c), and (i) from area of (d) [taken from ref. [64] with permission from RSC].

Figure 16 a) Schematic of the 3D solid state interpenetrating cell; b) SEM micrograph of a cell cross-section after cycling showing the pore filling with the V_2O_5 ambigel cathode [taken from ref. [66] with permission from ECS].

Figure 17- FESEM images of (a)–(c) TiO2 nanowire arrays and (d)–(f) TiO_2 nanowire@Fe_2O_3 nanothorn core–branch arrays; g) Rate performances of the TiO_2@Fe_2O_3 hybrid array electrode and the TiO_2 nanowire array electrode [taken from ref. [69] with permission from Springer].

Figure 18- a) HAADF STEM of a NWLIB on SiNx; b) a FIB cut cross section FESEM image and c) schematic [taken from ref. [74] with permission from ACS].

Figure 19- a) An exploded schematic view of the microbattery components. The cathode is attached inside a gold ‘‘can’’ using conductive carbon, while the lithium foil anode is attached to the copper

lid. A film of insulating Li–P–O–N glass is deposited onto the can flanges. An intervening microporous separator is placed between the flange and the lid. The two halves of the cell are sealed using a fast-setting, photocured adhesive; b) Packaged microbattery compared to US penny; c) volumetric energy density plotted versus battery volume for selected commercially available technologies. The powder density indicated were achieved under constant current discharge of the microbatteries at C/3 and C/2 rates after being charged at C/20-C/10 rates. The blue and red closed circles correspond to cells charged to voltages of 4.6 and 4.5V respectively [taken from ref. [78] with permission from Wiley].

Figure 20- a) Cartoon representation of the sequential steps that can generate an integrated nanocomposite with interpenetrating electrodes: formation of a monolithic manganese oxide ambigel nanoarchitecture showing the oxide network (red, 1st step) onto which a conformal ultrathin polymer separator/electrolyte (blue, 2nd step) has been electrodeposited. Within the residual interconnected free volume, a counter insertion electrode (nanoscopic RuO_2, green, 3rd step) has been infiltrated; b) TEM micrograph of MnO_x‖PPO after deposition of nanoscopic RuO_2 via decomposition of RuO_4 [taken from ref. [79] with permission from RSC].

Figure 21- a) SEM image of a cross-section of laser structured $LiCoO_2$ thin film deposited on a silicon substrate (wavelength λ = 248 nm, laser fluence ε = 1.0 J/cm², repetition rate νrep = 100 Hz, laser pulse number n = 50, processing gas: helium, substrate: silicon) [taken from ref. 83 with permission from INOE]; b) SEM image overview (c) and cross-sectional polish of a laser structured tape-cast $LiCoO_2$ electrode. A laser fluence of 1.5 J/cm^2, 500 laser pulses and a repetition rate of 300 Hz were used [taken from ref. [80] with permission from Springer].

Figure 22- a) Flow chart summarizing the experimental procedure, key results and the overall performance for the laser printed/laser structured $LiMn_2O_4$ thick films; SEM images of b) and c) laser printed $LiMn_2O_4$ thick film before calendaring showing active particles and active particles coating with carbon black and binder, d) and e) of un-calendered and calendered laser structured cathodes [taken from ref. [81] with permission from Elsevier].

Figure 23- a) Schematic illustration of the 3D printed interdigitated microbattery; b) SEM images of printed and annealed 16-layer interdigitated LTO-LFP electrode architecture; c) picture of the 3D printed microbattery after packaging; d) areal capacity of a full cell composed of 8-layer interdigitated LTO-LFP electrode architecture [taken from ref. [7] with permission from Wiley].

Figures

Figure 1

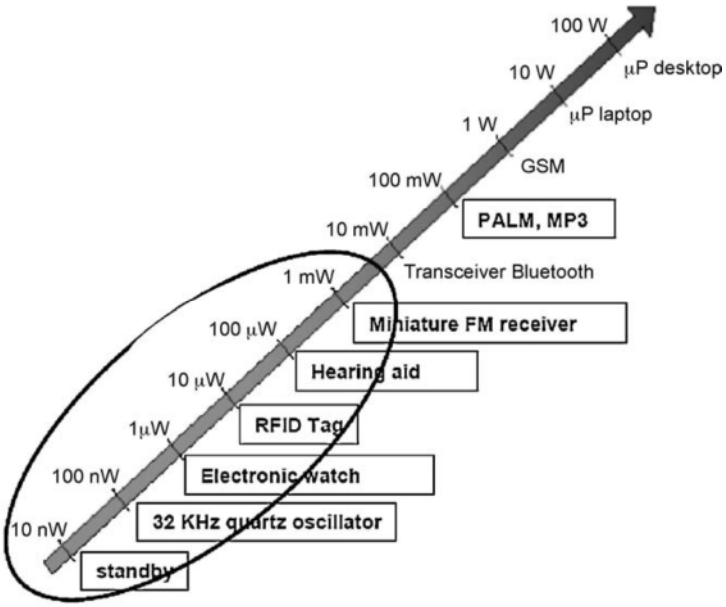

Figure 2

a)

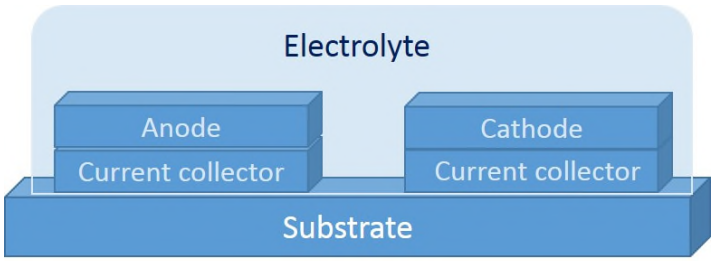
Electrolyte
Anode
Current collector
Cathode
Current collector
Substrate

b)

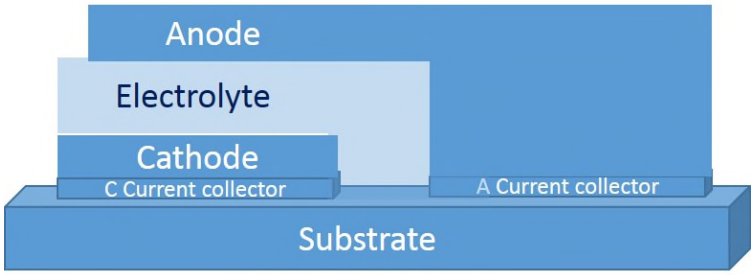
Anode
Electrolyte
Cathode
C Current collector
A Current collector
Substrate

Figure 3

a)

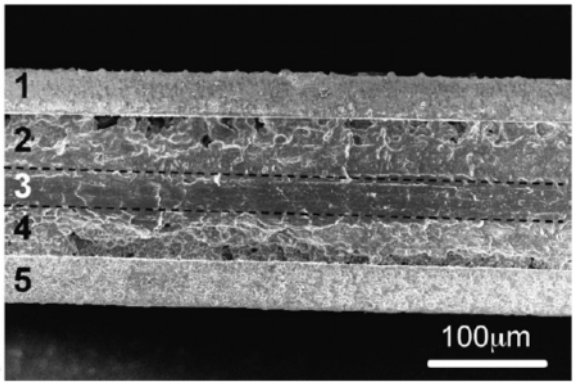

b)

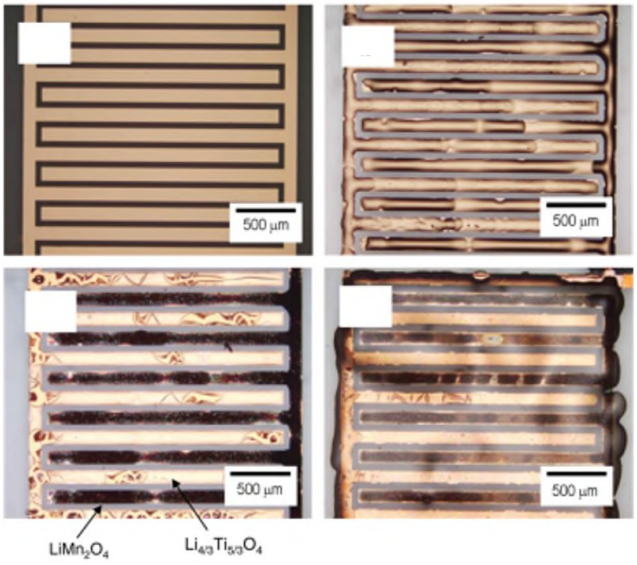

Figure 4

a)

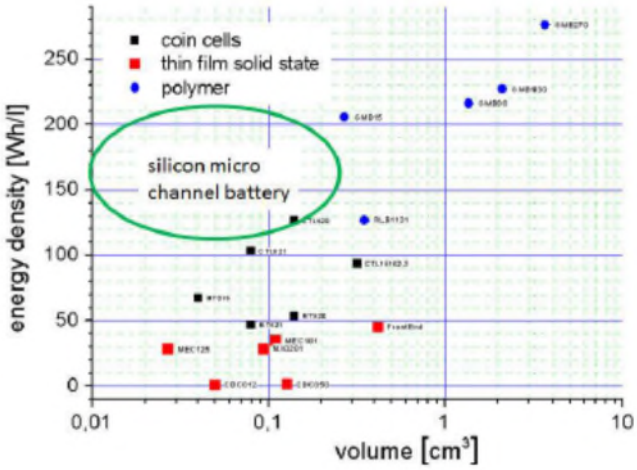
coin cells
thin film solid state
polymer
silicon micro
channel battery
energy density [Wh/l]
250
200
150
100
50
0
0,01
0,1
1
10
volume [cm³]

b)

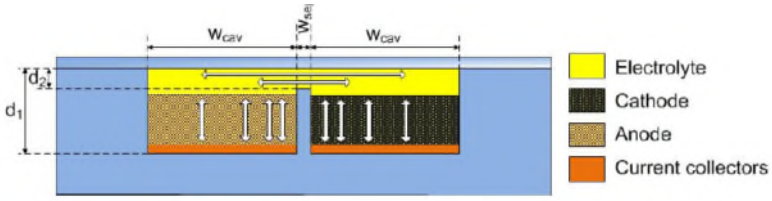
Electrolyte
Cathode
Anode
Current collectors

c)

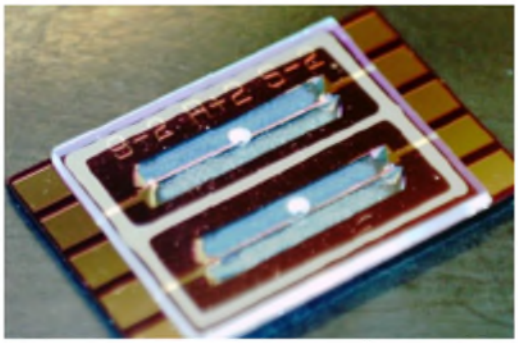

Figure 5

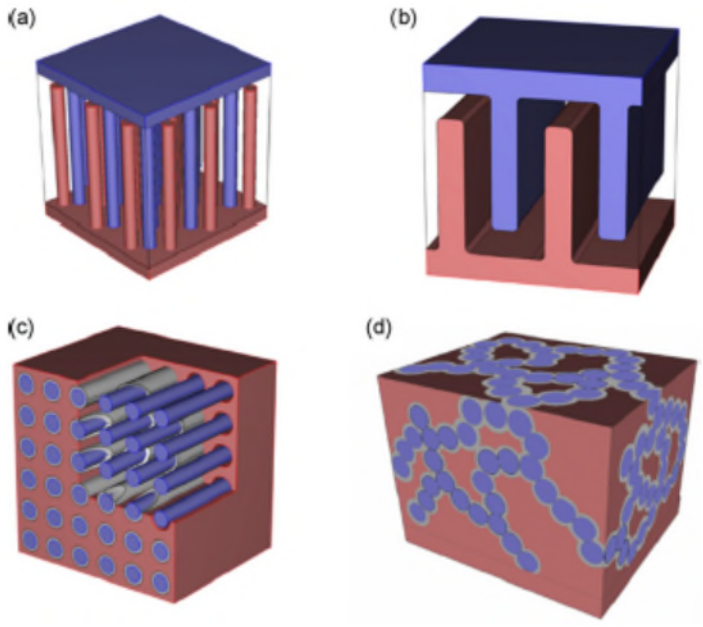

Figure 6

a)

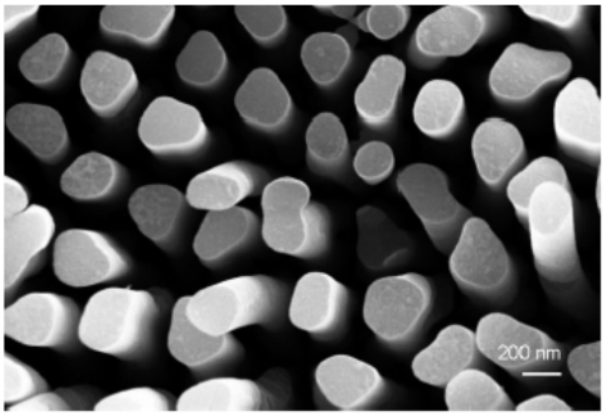

b)

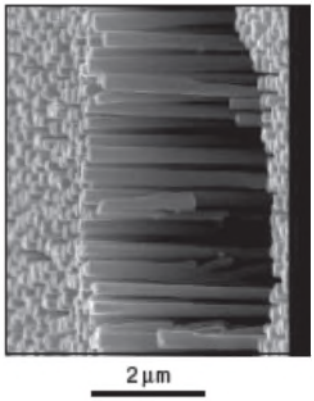

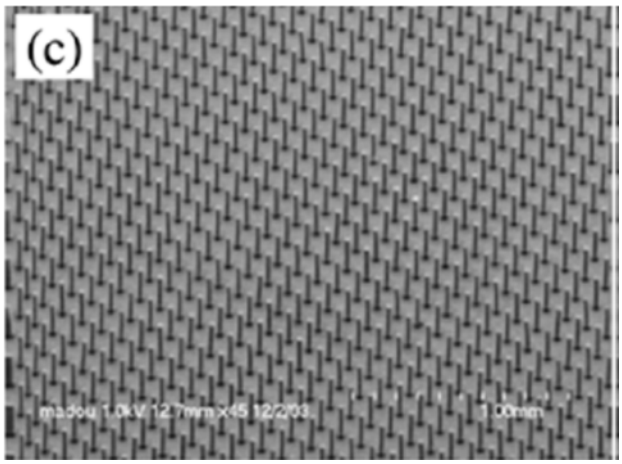

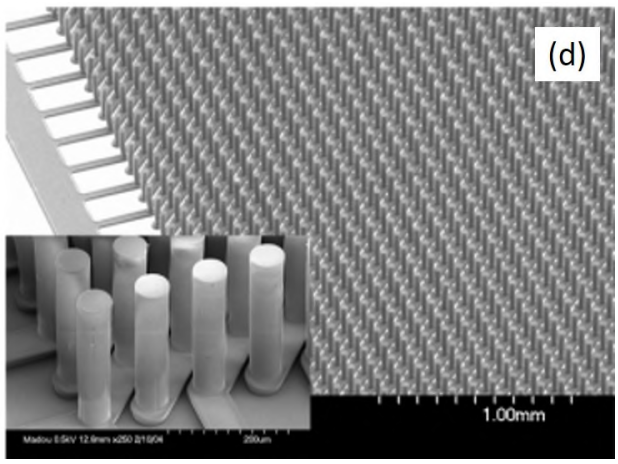

Figure 7

a)

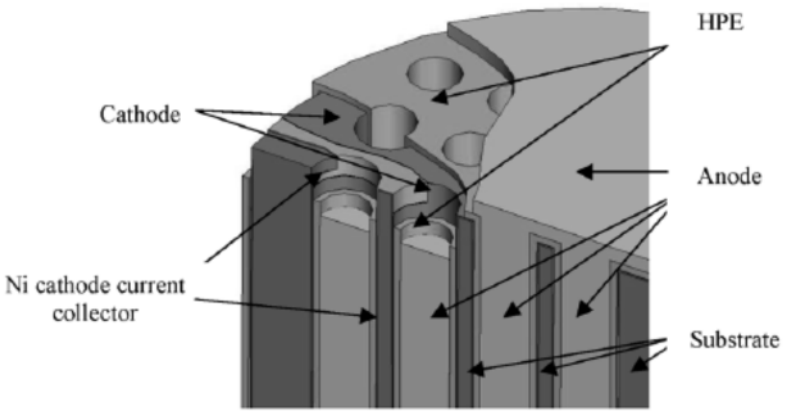
HPE
Cathode
Anode
Ni cathode current collector
Substrate

b)

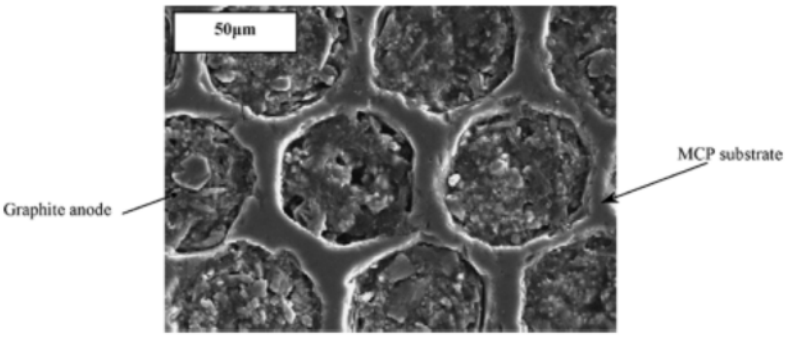
50µm
MCP substrate
Graphite anode

c)

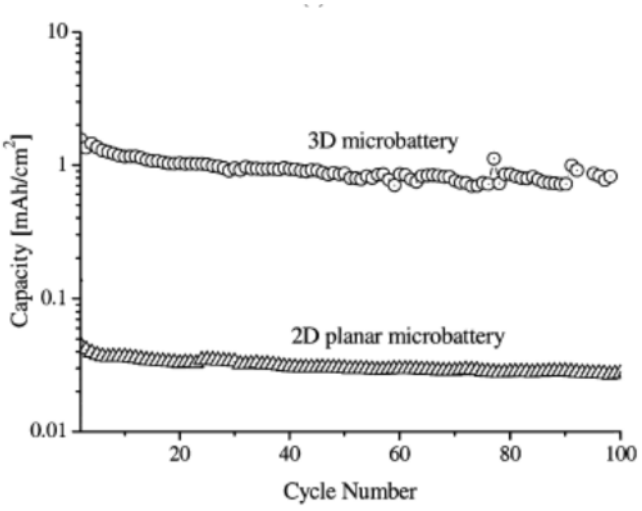
10
1
0.1
0.01
Capacity [mAh/cm²]
3D microbattery
2D planar microbattery
20
40
60
80
100
Cycle Number

Figure 8

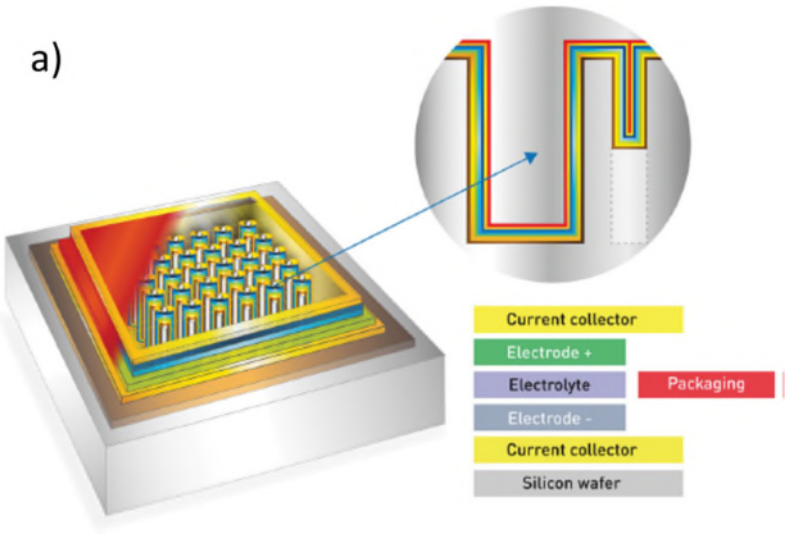
a)
Current collector
Electrode +
Electrolyte
Packaging
Electrode -
Current collector
Silicon wafer

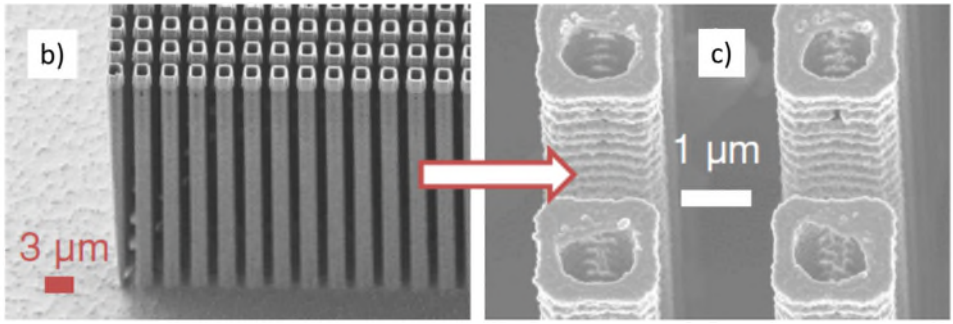
b)
3 µm
c)
1 µm

Figure 9

a)

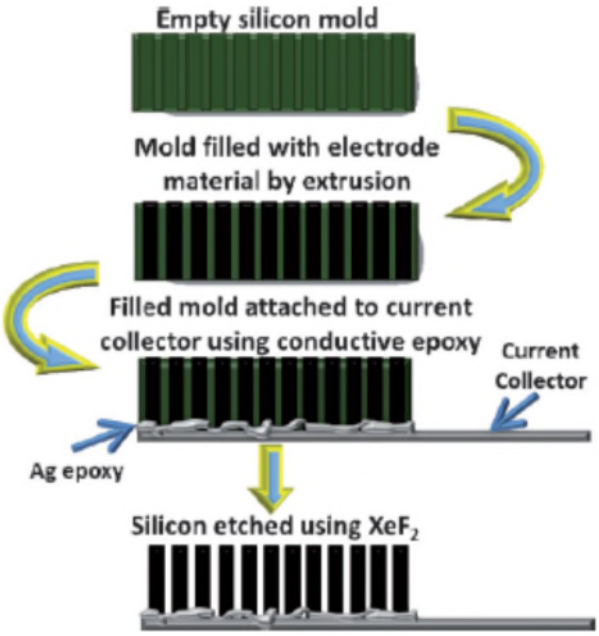
Empty silicon mold
Mold filled with electrode material by extrusion
Filled mold attached to current collector using conductive epoxy
Current Collector
Ag epoxy
Silicon etched using XeF_2

b)

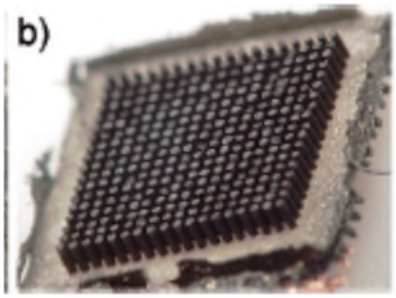

Figure 10

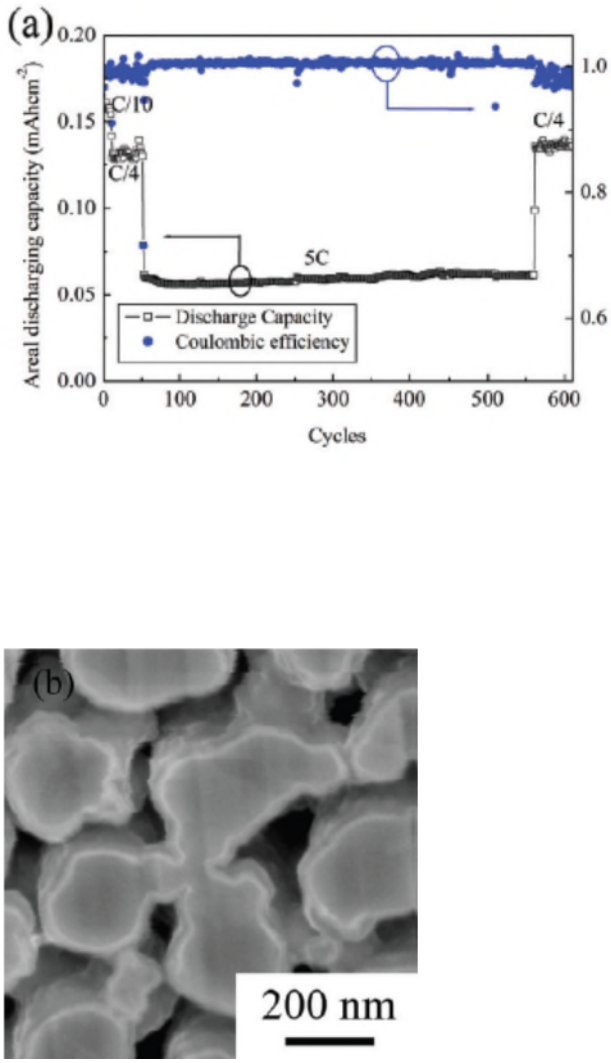
(a)
Areal discharging capacity (mAhcm^{-2})
Cycles
C/10
C/4
5C
C/4
Discharge Capacity
Coulombic efficiency
0.00
0.05
0.10
0.15
0.20
0.6
0.8
1.0
0
100
200
300
400
500
600
(b)
200 nm

Figure 11

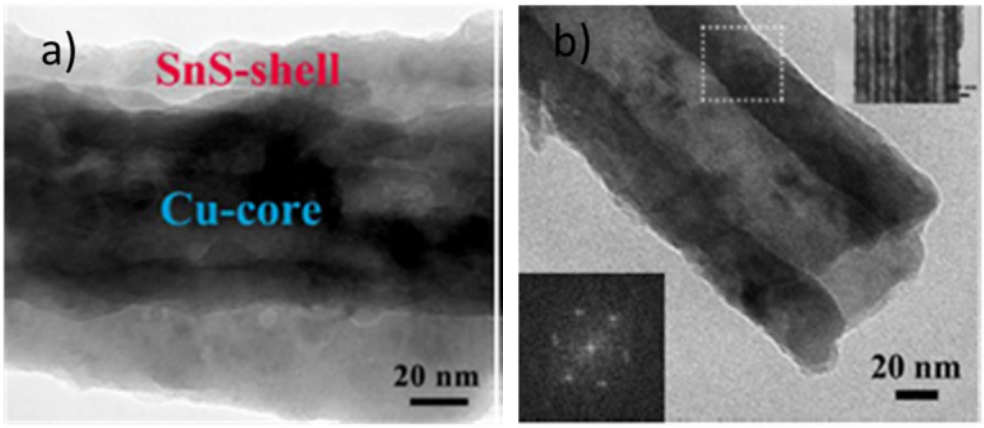
a)
SnS-shell
Cu-core
20 nm
b)
20 nm

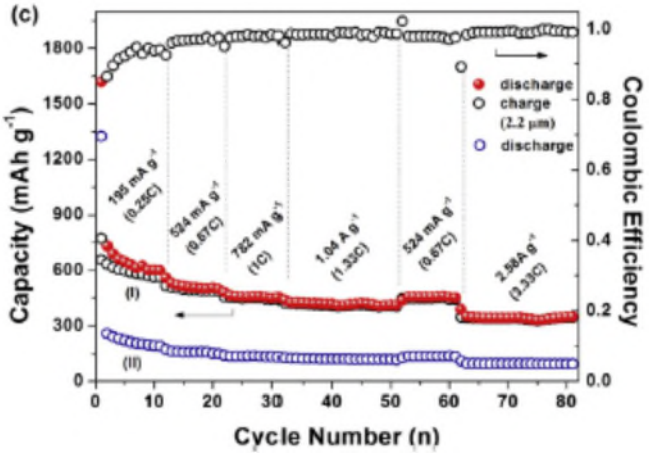
(c)
Capacity (mAh g-1)
Coulombic Efficiency
Cycle Number (n)
discharge
charge
(2.2 μm)
discharge
195 mA g-1 (0.25C)
524 mA g-1 (0.67C)
722 mA g-1 (1C)
1.04 A g-1 (1.33C)
524 mA g-1 (0.67C)
2.56A g-1 (3.33C)
(I)
(II)

Figure 12

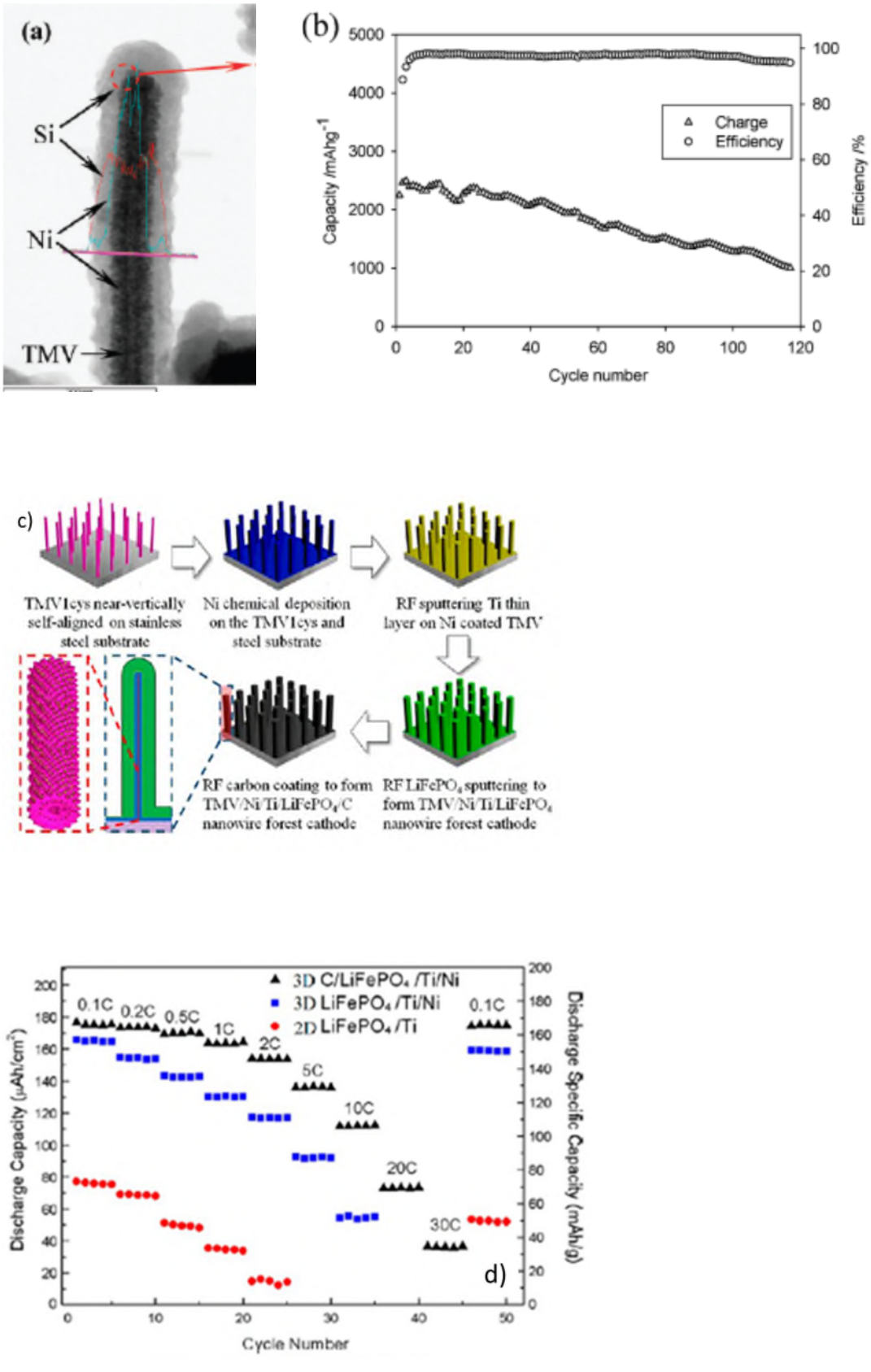
(a)
Si
Ni
TMV
(b)
Capacity /mAhg-1
Efficiency /%
Cycle number
Charge
Efficiency
c)
TMV1cys near-vertically self-aligned on stainless steel substrate
Ni chemical deposition on the TMV1cys and steel substrate
RF sputtering Ti thin layer on Ni coated TMV
RF LiFePO4 sputtering to form TMV/Ni/Ti/LiFePO4 nanowire forest cathode
RF carbon coating to form TMV/Ni/Ti/LiFePO4/C nanowire forest cathode
3D C/LiFePO4 /Ti/Ni
3D LiFePO4 /Ti/Ni
2D LiFePO4 /Ti
0.1C
0.2C
0.5C
1C
2C
5C
10C
20C
30C
0.1C
d)
Discharge Capacity (μAh/cm2)
Discharge Specific Capacity (mAh/g)
Cycle Number

Figure 13

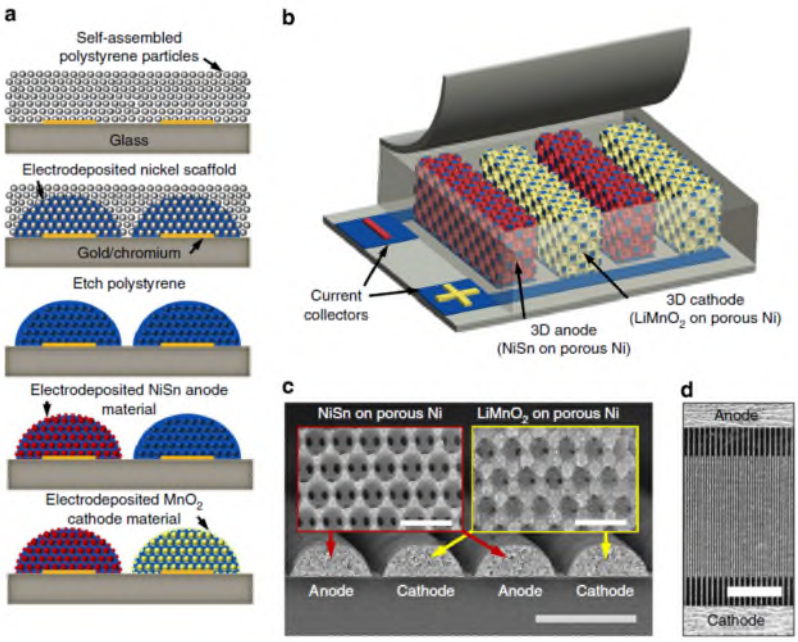
a
Self-assembled polystyrene particles
Glass
Electrodeposited nickel scaffold
Gold/chromium
Etch polystyrene
Electrodeposited NiSn anode material
Electrodeposited MnO_2 cathode material
b
Current collectors
3D anode (NiSn on porous Ni)
3D cathode ($LiMnO_2$ on porous Ni)
c
NiSn on porous Ni
$LiMnO_2$ on porous Ni
Anode
Cathode
Anode
Cathode
d
Anode
Cathode

Figure 14

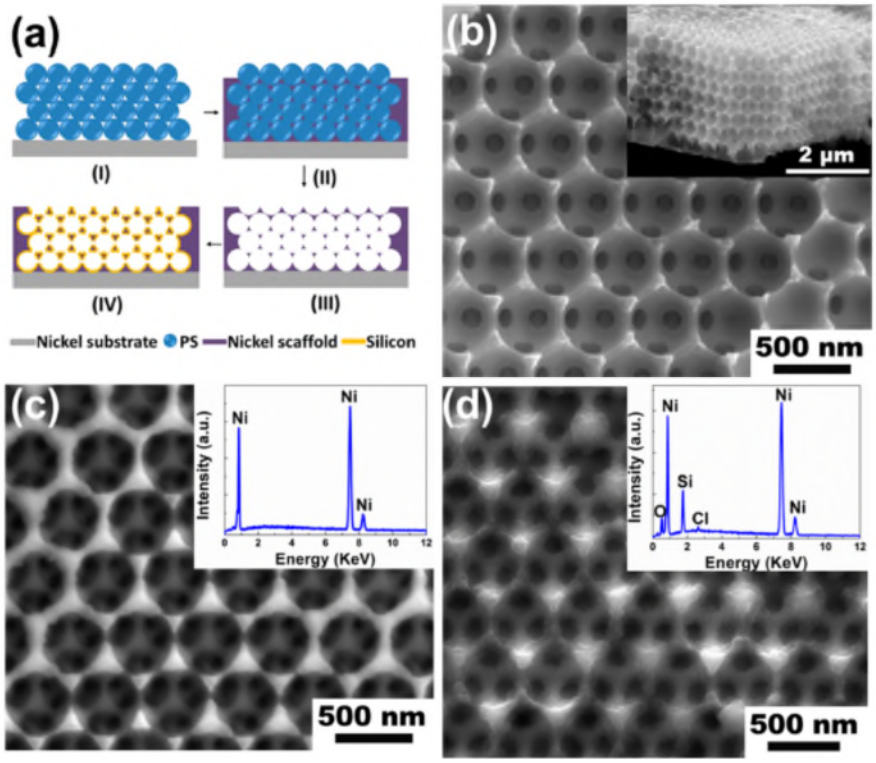
(a)
(I)
(II)
(III)
(IV)
Nickel substrate
PS
Nickel scaffold
Silicon
(b)
2 μm
500 nm
(c)
Ni
Ni
Ni
Intensity (a.u.)
Energy (KeV)
500 nm
(d)
Ni
Ni
Si
Cl
Ni
O
Intensity (a.u.)
Energy (KeV)
500 nm

Figure 15

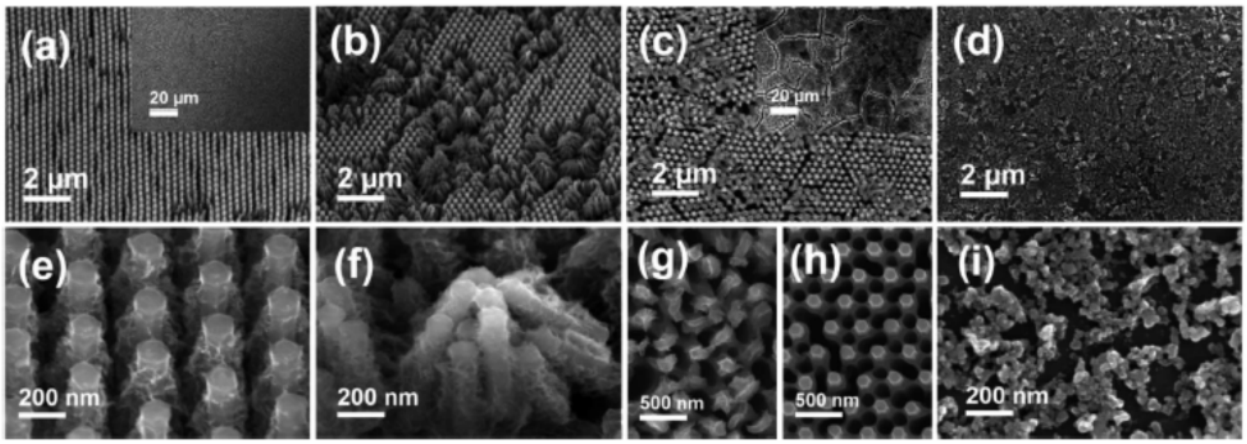
(a)
20 μm
2 μm
(b)
2 μm
(c)
20 μm
2 μm
(d)
2 μm
(e)
200 nm
(f)
200 nm
(g)
500 nm
(h)
500 nm
(i)
200 nm

Figure 16

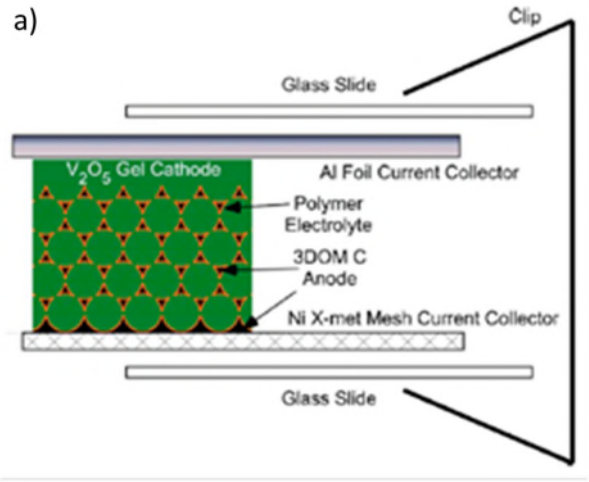
a)
Clip
Glass Slide
V_2O_5 Gel Cathode
Al Foil Current Collector
Polymer
Electrolyte
3DOM C
Anode
Ni X-met Mesh Current Collector
Glass Slide

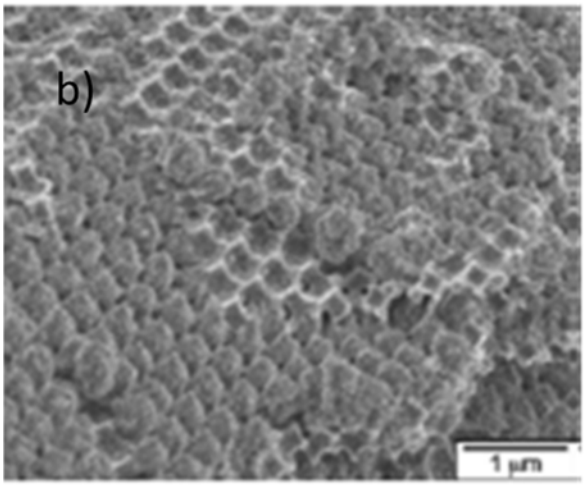
b)
1 µm

Figure 17

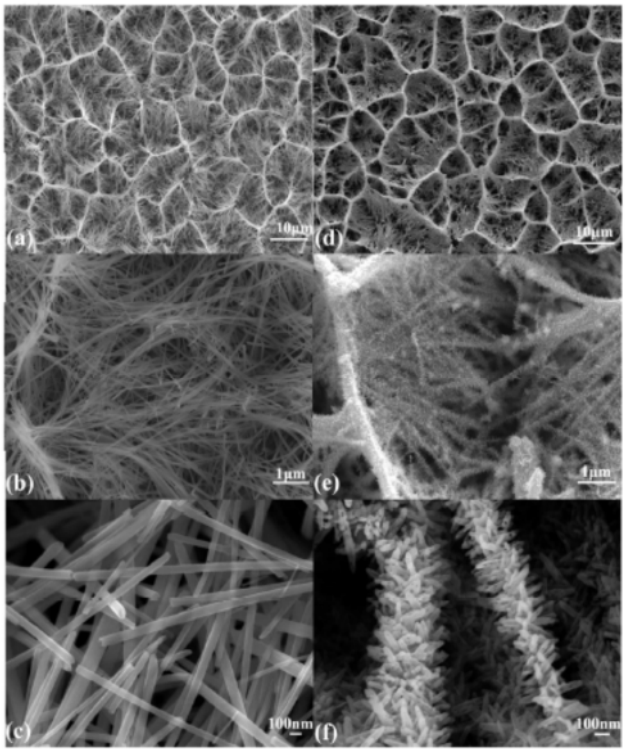
(a)
10μm
(d)
10μm
(b)
1μm
(e)
1μm
(c)
100nm
(f)
100nm

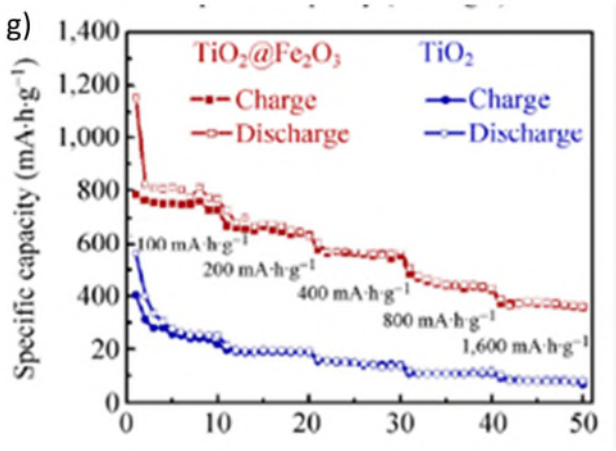
g)
Specific capacity (mA·h·g⁻¹)
1,400
1,200
1,000
800
600
400
20
0
0
10
20
30
40
50
TiO2@Fe2O3
Charge
Discharge
TiO2
Charge
Discharge
100 mA·h·g⁻¹
200 mA·h·g⁻¹
400 mA·h·g⁻¹
800 mA·h·g⁻¹
1,600 mA·h·g⁻¹

Figure 18

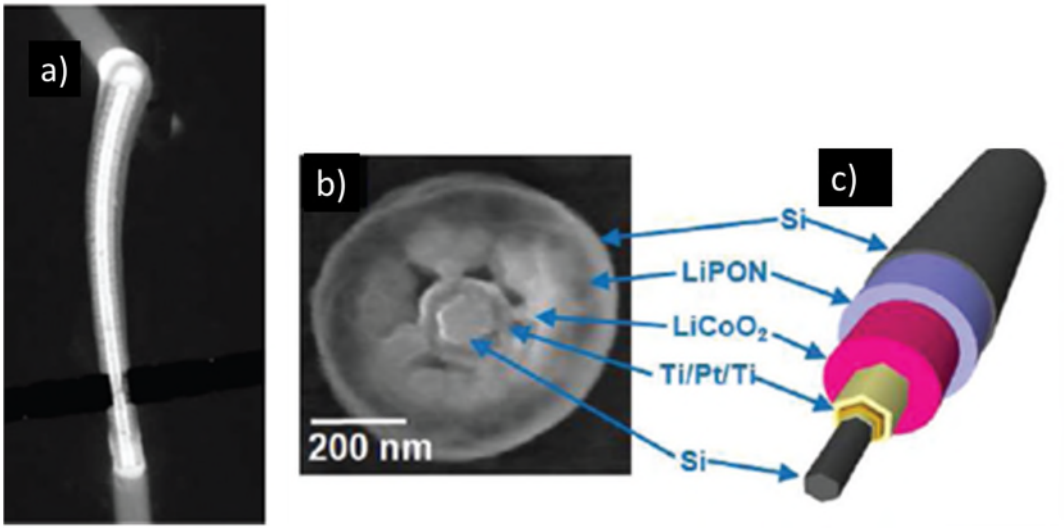

Figure 19

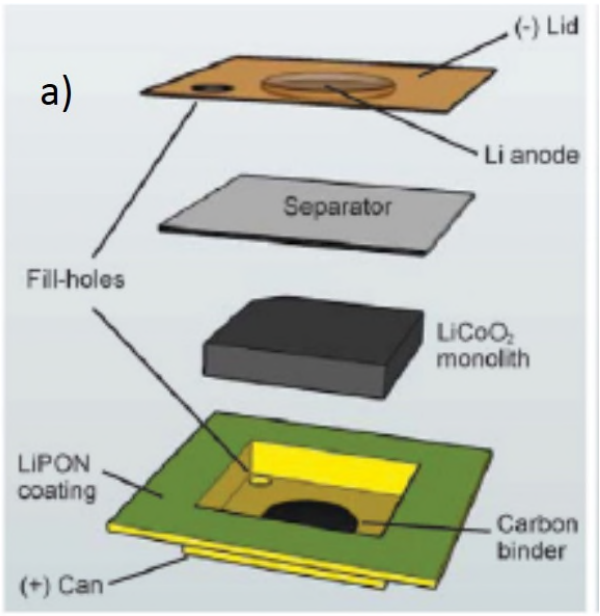
a)
(-) Lid
Li anode
Separator
Fill-holes
$LiCoO_2$ monolith
LiPON coating
Carbon binder
(+) Can


b)
LIBERTY

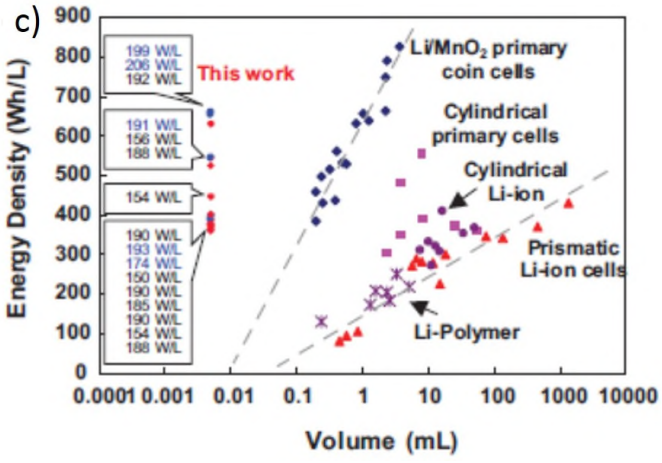
c)
Energy Density (Wh/L)
Volume (mL)
0.0001
0.001
0.01
0.1
1
10
100
1000
10000
0
100
200
300
400
500
600
700
800
900
199 W/L
206 W/L
192 W/L
This work
191 W/L
156 W/L
188 W/L
154 W/L
190 W/L
193 W/L
174 W/L
150 W/L
190 W/L
185 W/L
190 W/L
154 W/L
188 W/L
Li/MnO_2 primary coin cells
Cylindrical primary cells
Cylindrical Li-ion
Prismatic Li-ion cells
Li-Polymer

Figure 20

a) b)

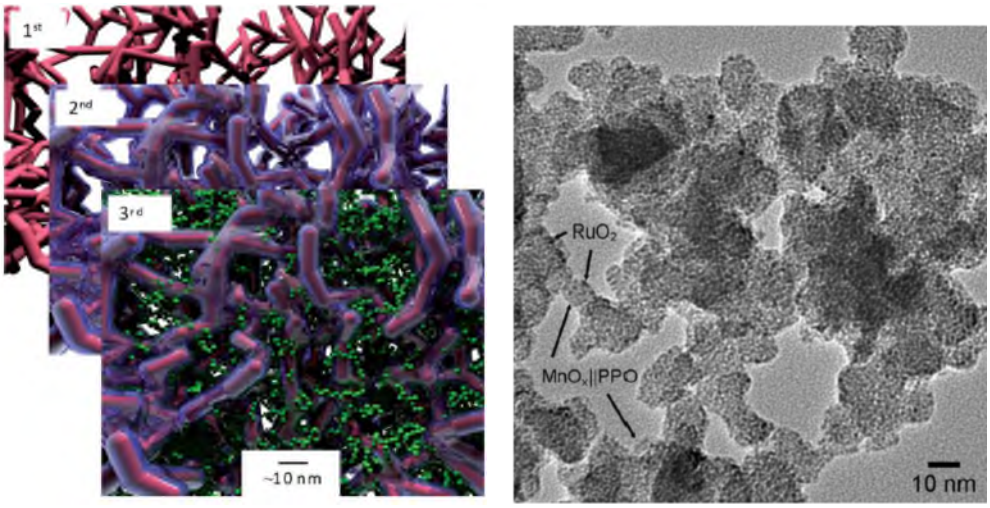

Figure 21

a)

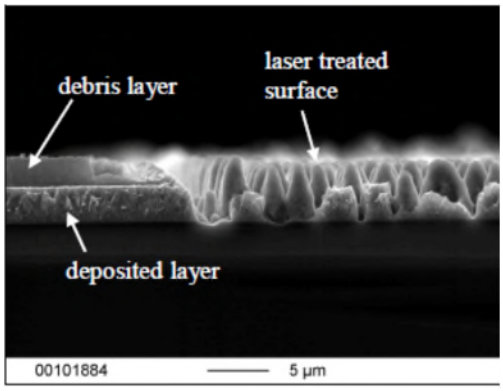

b)

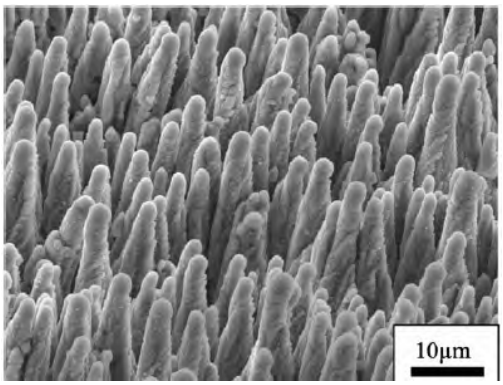

c)

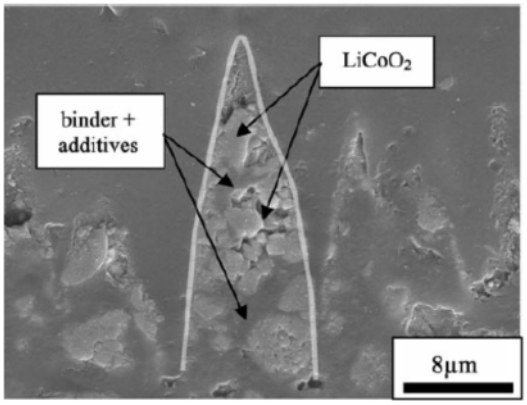

Figure 22

a)

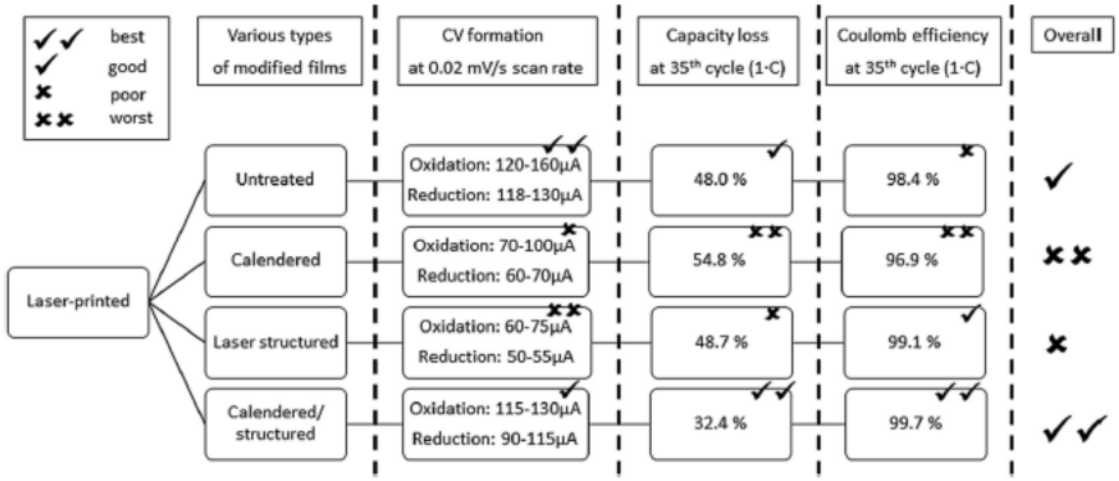

b)

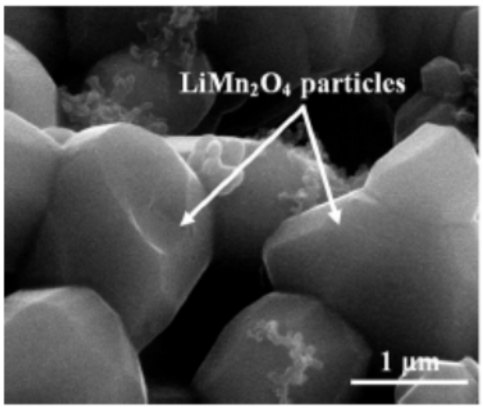

c)

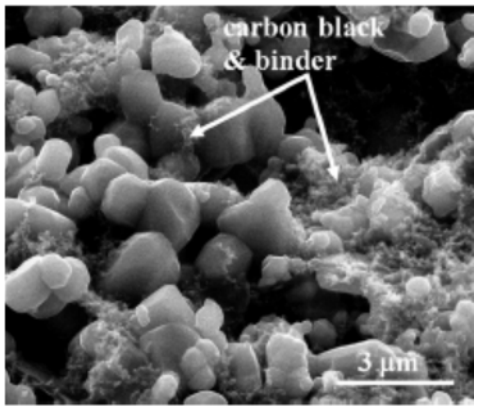

d)

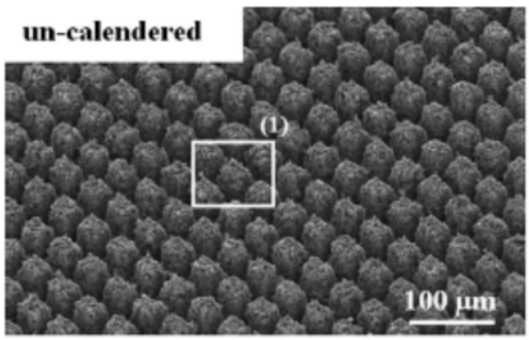

e)

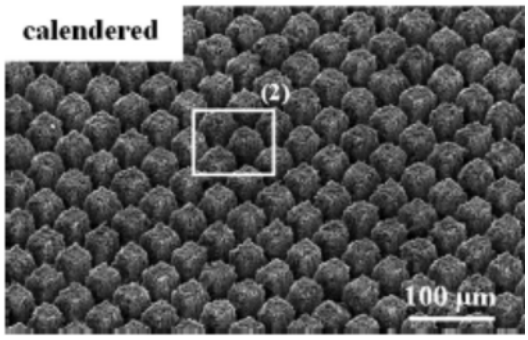

Figure 23

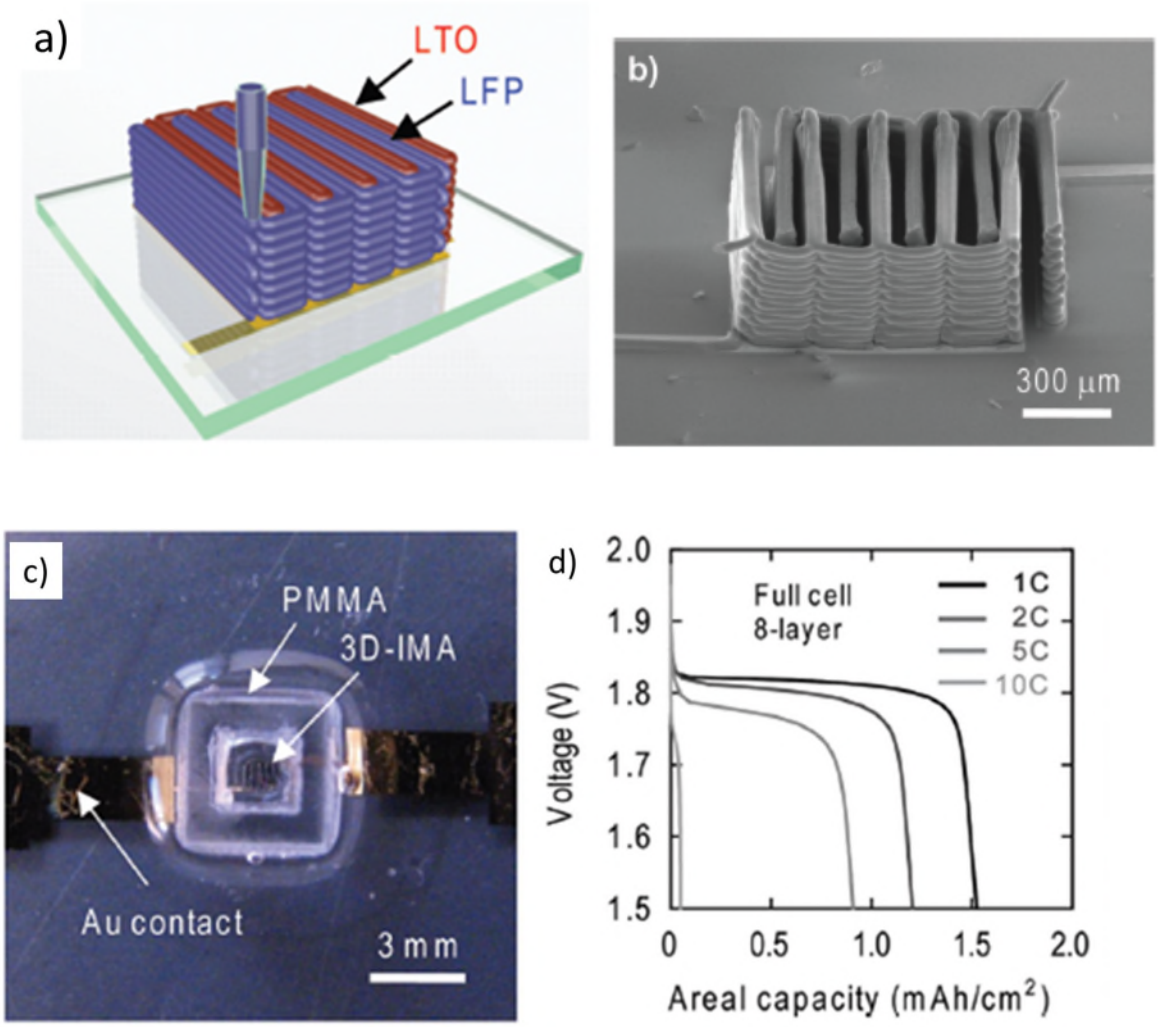
a)
LTO
LFP
b)
300 μm
c)
PMMA
3D-IMA
Au contact
3 mm
d)
Full cell
8-layer
1C
2C
5C
10C
Voltage (V)
2.0
1.9
1.8
1.7
1.6
1.5
0
0.5
1.0
1.5
2.0
Areal capacity (mAh/cm²)